

Ultra Portable and Rapidly Deployable Rotorcraft Platform for Tactical Compact Communications Relay

A project present to
The Faculty of the Department of Aerospace Engineering
San Jose State University

in partial fulfillment of the requirements for the degree
Master of Science in Aerospace Engineering

By

Ben E. Nikaido

December 2013

approved by



Dr. Nikos Mourtos
Faculty Advisor



San José State
UNIVERSITY

ABSTRACT

This report includes the motivation for and preliminary design of a man-portable, rapidly-deployable, and cost-effective rotorcraft platform to carry a communication relay payload. A quadrotor design with 0.427 meter (16.8 inch) diameter rotors was chosen. The estimated weight of the aircraft is 1.471 kilograms. Rotor momentum theory yields and estimated quadrotor vehicle hover endurance of 21 minutes. CFD and experimental analysis was conducted to evaluate rotor design at low operational Reynolds numbers. CFD (using the CFD-ACE+ code) showed slight efficiency gains of cambered plated designs at lower rotational speeds over traditional airfoils. Experimental testing yielded better performance of a commercial-off-the-shelf (COTS) flat-plate rotor over the streamlined airfoil rotor of a larger diameter.

Faculty Adviser:



Dr. Nikos Mourtos

Director, Aerospace Engineering

San Jose State University

Advisory Committee:


Larry Young
NASA Ames Research Center

 12/16/2013
Satish Chetty
Beyond 66

ACKNOWLEDGEMENTS

I wish to thank my Aerospace Engineering faculty, Dr. Mourtos and Dr. Papadopoulos, for the many fun and challenging years and inspiring me to pursue this stage of higher education. I also wish to express my sincere gratitude to my technical advisory committee, Larry Young and Satish Chetty, for which this project would not be possible. On numerous occasions, Larry kindly invited me to NASA Ames to share his immense knowledge of rotorcraft, direct me during research, guide me through the engineering process. I am also grateful for the time Larry sacrificed to increase the accuracy and professionalism of this report. I am thankful to Satish for the years of assistance in and inspiration for electronics and robotics.

Contents

1.0 INTRODUCTION.....	1
1.1 MISSION.....	3
1.2 SCOPE OF PROJECT.....	5
1.3 TECHNICAL TASKS.....	5
1.4 TECHNICAL CHALLENGES.....	6
2.0 CONCEPTUAL AND PRELIMINARY DESIGN.....	7
2.1 PLATFORM CONFIGURATION.....	7
2.2 VEHICLE SIZING AND PACKAGING/STOWING.....	8
2.3 WEIGHT ESTIMATE.....	11
2.4 HOVER POWER ESTIMATE.....	12
2.5 ENDURANCE ESTIMATE.....	13
3.0 PROOF-OF-CONCEPT (POC) DEVELOPMENT.....	14
4.0 CHALLENGES IN IMPROVING VEHICLE HOVER EFFICIENCY AND ENDURANCE.....	16
4.1 AIRFOILS AND ROTORS OPERATING IN THE LOW REYNOLDS NUMBER REGIME.....	17

4.2 BOUNDARY LAYERS ON AIRFOILS.....	19
4.3 LAMINAR SERARATION BUBBLE.....	20
4.4 AIRFOIL BEHAVIOR.....	21
5.0 ROTOR AERODYNAMICS AND HOVER PERFORMANCE.....	25
5.1 BLADE ELEMENT THEORY.....	25
5.2 BLADE ELEMENT MOMENTUM (BEM) THEORY.....	27
5.3 BEM ROTOR ANALYSIS.....	28
6.0 ROTOR CFD ANALYSIS.....	30
6.1 APPROACH.....	31
6.2 CFD RESULTS.....	35
7.0 EXPERIMENTAL ROTOR TESTING.....	39
7.1 EXPERIMENTAL RESULTS.....	41
8.0 CONCLUSIONS.....	45
TO CONCLUDE.....	45
REFERENCES.....	46

1.0 INTRODUCTION

In June of 2005, Navy SEAL Lieutenant Michael P. Murphy and his team were on a covert mission to find and monitor a Taliban leader deep in the mountains of Afghanistan. Taliban militants became aware of the SEAL's plans and subsequently ambushed them with heavy fire, forcing the American soldiers into a canyon. Because the mountainous terrain restricted line-of-sight (LOS) radio communication, the SEALs were unable to call for air support. Lt. Murphy, determined to make the call, ventured out of the canyon and knowingly into the plain sight of the opposition. While under continuous fire, and incurring a shot to his back, Murphy succeeded in placing a call to headquarters. Unfortunately, afterwards, Lt. Murphy, the majority of his SEAL team, and a large number of responding backup troops were killed by Taliban forces. Lt. Murphy was awarded the Congressional Medal of Honor for his heroic actions and sacrifice. [5]

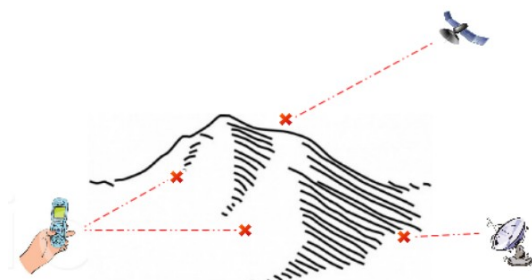


Figure 1: Line-of-Sight obstructed by terrain.

Boeing Electronic and Mission Systems has recently developed a partial solution to the LOS problem, as shown in Figure 1, which plagued Lt. Murphy and still plagues warfighters in similar dire situations. The Tactical Compact Communications Relay (TCCR) is a small, yet highly capable, electronic module that acts as a relay for military and emergency response radio communication systems. In theater since July 2011, the TCCR weighs 1 lb, is smaller than 37 cubic inches in size, and can theoretically extend the range of radio communications to over 160 nautical miles. Aerial platforms currently carrying the TCCR include the Boeing/Insitu Scan Eagle, the AeroVironment Puma, the S-100 rotorcraft, and aerostats. [6] The Scan Eagle, S-100, and Puma are shown in Figures 2a-c, respectively. All of the previously mentioned aircraft require significant planning and infrastructure to launch and most cannot be freely carried by ground troops on tactical missions. The smallest known UAV platform to house the TCCR is the AeroVironment Puma. Although man-portable and hand-launched, the Puma requires a full-time human operator, is susceptible to inclement weather and wind, and cannot fit into a standard military backpack.



Figure 2a: Insitu Scan Eagle. [12]



Figure 2b: Schiebel S-100. [13]



Figure 2c: Aeroviroment Puma. [14]

Several other technologies are being evaluated to solve the LOS problem in areas of military conflict. The Department of Defense (DoD) has growing interest in autonomous high-altitude airships as a surveillance platforms and also as communications relays. Although such airships could remain aloft for weeks at a time, they have their own drawbacks including a substantial financial penalty (millions of dollars per aircraft), significant support infrastructure required for logistics, and presenting a relatively easy and ever-present target to potential adversaries with resources to take them down. Another option currently being considered is the capability to rapidly put satellites into orbit over areas of conflict or interest. The military's Operationally Responsive Space (ORS) office has been attempting to develop the capability to deploy small and cheap satellites in only weeks based on emerging tactical needs. This is rather attractive compared to the years it traditionally takes to develop satellites. Unfortunately, the ORS has had only marginal success since it's conception in 2007.

Therefore, the overall objective of this thesis is to consider a unique aerial asset that could potentially carry the TCCR relay as a payload and, thereby, solve the LOS problem for the warfighter and the first responder. The particular aerial asset needs to be man-portable – in fact needs to be able to be carried in a standard soldier's backpack. Should such a platform exist, or be created, that is compact and affordable enough such that it could be carried by anyone that may encounter a need for a communications relay, the potential to accomplish missions and save lives in critical circumstances is greatly improved. The conceptual vehicle of choice is a small quadcopter/quadrotor rotary-wing platform. The remaining portion of the thesis will consider this vehicle -- and its rotor efficiency and performance -- in the context of enabling an effective LOS solution.

1.1 MISSION

The proposed mission is to design and demonstrate a man-portable, rapidly-deployable, and cost-effective aircraft platform to carry the TCCR or similar device. The nature of the aircraft's flight is relatively simple: it should be capable of being hand-launched, or takeoff directly from the ground, with minimal takeoff distance required; it must simply gain altitude until it could satisfy LOS communication, as shown in Figure 3; it must be hover or loiter at altitude to establish and maintain the LOS communications relay. Although the original inspiration for the platform is tactical in nature, it should be noted that it could also be equally useful for situations outside of the military, including outdoorsmen and first-response personnel. For these applications the aircraft could be outfitted with a cellular and/or civil radio relay in place of the TCCR.

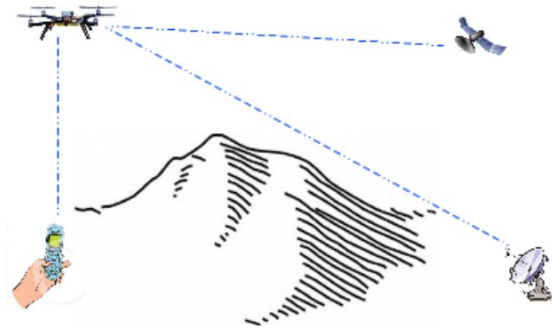


Figure 3: Aerial relay platform enabling LOS to receiver and/or satellite, solving the obstruction problem as shown in Figure 1.

In contrast to the existing aircraft mentioned earlier that have carried the TCCR as a payload, the aerial vehicle to be considered in this study will require little to no input from the operator. This semi-autonomous feature would enable the user to give the task at hand – i.e. establishing radio transmission - his/her undivided attention - without having to concurrently remote-pilot/operate a small aerial platform. The ability to “launch and forget” a relay may have proven priceless for Lt. Murphy while under a hailstorm of enemy fire.

A set of objectives that define measures of mission/vehicle success are outlined below. The objectives are ranked in three discrete levels: minimum, intermediate, and optimal. The set of minimum objectives would yield an initial operating capability for the vehicle/mission. Performance values outlined are assuming sea level and standard day temperature and pressure. The more challenging intermediate and optimal sets of objectives would greatly enhance the overall mission capability. The work for this study will mostly focus on the challenges of meeting the minimum objectives.

Minimum Objectives:

- The aircraft must be able to, upon operator command, ascend vertically to 50 ft above ground level (AGL) and sustain 15 minutes or more of hovering flight.
- The aircraft must carry a 1 lb payload and provide the requisite power for operating the TCCR module or equivalent device for the endurance of the flight.
- The aircraft must fit into a standard 18" (1296 cubic inches) backpack in either collapsed or flight-ready configuration.

Intermediate Objectives:

- The aircraft must be able to, upon operator command, ascend to an altitude of 150' AGL at a maximum of 10000' density altitude.
- The hovering endurance must exceed 20 minutes upon reaching target altitude.



Figure 4: Flight profile for minimum and intermediate objectives.

Optimal Objectives:

- The aircraft must be able to be launched and "forgot" by the operator, minimizing operator intervention.
- The aircraft must consume only half the space of a standard size backpack in either collapsed or flight-ready configuration.

- Hover endurance must be at least 30 minutes.
- After launch and while ascending to the required altitude, the aircraft must be able to autonomously dodge obstacles such as canyon walls, cliff faces, and other types of rock formations.
- The aircraft must autonomously ascent to an altitude and location that is in line-of-sight of both the sender and receiver.
- The aircraft must be able to maintain required position under windy and gusty condition.
- If in a hostile environment, the aircraft must autonomously fly randomly so as not to give away the sender's position on the ground.
- It must autonomously return to the sender after mission or land/fall in a relatively distant location so to keep the sender's location discrete.

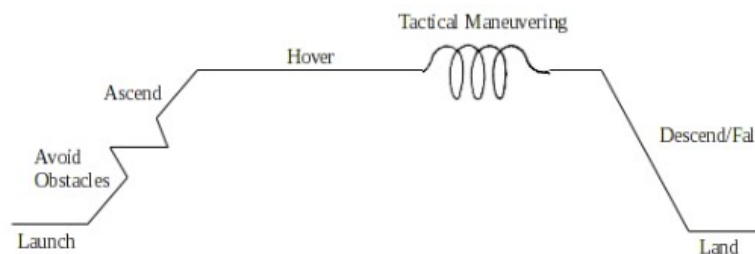


Figure 5: Flight profile for optimum objectives.

1.2 SCOPE OF PROJECT

This project will encompass designing, developing, and testing a rotorcraft platform that carries a previously working communications relay. In particular, small quadrotor/quadcopter vehicles will be considered. One key reason for this choice is that existing commercial-off-the-shelf (COTS) quadcopter vehicles already have many of the required attributes for the LOS mission. For example, sophisticated avionics, and ease of control, make this type of aerial vehicle very accessible to novice operators. Additionally, many open-source software/hardware projects have demonstrated semi- and fully-autonomous vehicles of this type. Finally, low-cost systems are already commercially available. This study's conceptual design phase will conclude with include with both a computational and experimental thorough aerodynamic assessment, analysis

and performance optimization, of the aircraft's lifting rotors that meets leads to the targeted vehicle endurance goals.

1.3 TECHNICAL TASKS

The following is a list of technical tasks that will be cultivated during the course of this study to meet the identified mission specifications/objectives:

- Design an airframe that could carry the requisite payload and reduce in size and weight to ensure total man-portability.
- Significantly improve the quadcopter flight endurance. Since the majority of the flight will be spent in hover, the focus will be on increasing the hover efficiency.

Equally important, but outside the scope of work performed, are the following tasks that are recommended for future work:

- Demonstrate a means of providing sufficient electric power to the TCCR, or similar device, for the entire duration of a mission-compatible flight.
- Develop the flight control system to provide a high-level of autonomy and minimal operator input. Launching the aircraft will consist of quickly bringing it into flight-ready configuration and simply switching the system on.
- Demonstrate that the TCCR or comparable communications relay, can be carried on a simulated mission and can – in mid-flight-- automatically find and maintain the appropriate geographic location and altitude that ensures transmissions between transmitter and receiver.

1.4 TECHNICAL CHALLENGES

The above lists of technical tasks present some unique technical challenges. Firstly, the rotorcraft's airframe will have to employ folding and/or telescoping members to comply with the

dimensional restrictions as outlined in the mission specifications. The mechanisms and joints must be robust, simple, lightweight, and enable quick transformation from packed to flight-ready configuration.

Improving the aircraft's hover efficiency will be accomplished by improving the rotor's aerodynamic efficiency as well as maintaining a lightweight airframe and efficient drivetrain(s). For a given high efficiency and RPM motor, the rotor could be optimized to produce the most amount of thrust with the least amount of rotational drag (torque). Theoretical models and computational fluid dynamics (CFD) will be utilized to obtain an efficient rotor design.

The system must autonomously attain and hold a position for the relay to be operational. This will require communication between the relay and the navigation and control system. There must be coded logic in the flight control computer that continuously attains input from the relay on whether or not the transmission is of requisite quality. If not, the system must quickly reach a location that does permit and sustain a reliable radio link between transmitter and receiver. There are several off-the-shelf complete flight control systems for small electric aircraft that permit at high-level of customization and programmable autonomy.

Lastly, there is ultimately a need to sense and avoid obstacles during climb to operating altitude, as well as possibly fly in a random/covert manner should the situation dictate such action, and maintain station keeping under adverse weather conditions. The sense and avoid feature will require integration of optical and/or sonar sensors with the flight control computer and the requisite logic. As mentioned above, many existing flight control systems are compatible with and have I/O ports for such sensors. Flying in an unpredictable manner while maintaining relay communication will require additional programming and relay-flight control computer integration. The aircraft and its systems will require weatherproofing to operate in heavy rain and snow. The stability and control system (integrated into most complete flight control systems) may require tweaking for the aircraft to fly to and maintain station in strong/gusty winds.

2.0 CONCEPTUAL AND PRELIMINARY DESIGN

2.1 PLATFORM CONFIGURATION

The primary factors driving the overall hardware design are:

- Compactness in portable configuration
- Hover efficiency (effective station-keeping)
- Simple and robust airframe
- Ease of transition from packet to flight-ready
- Ability to carry payload (relay)
- Low profile in tactical situations

Several configurations were considered in meeting these demands. A conventional helicopter (Figure 6a) satisfies five of the above criteria but requires an array of cams, pushrods, complex joints, and a tail rotor for control that greatly increase the amount of complexity and mechanical fragility. A coaxial rotor design (Figure 6b) does away with the tail rotor but still suffers from the same mechanical intricacies as the conventional helicopter. Figure 6b shows a less-common trirotor or “Y” design. This has an advantage over the previous two configurations in that it does not require as much control mechanisms, but still requires a method to tilt the rear rotor for yaw control. The quadrotor configuration as shown in Figure 6d satisfies all five of the design criteria and is the most mechanically elegant. A significant advantage with the quadrotor is that all of the vehicle's dynamics (yaw, pitch, roll, altitude, and translational flight) are controlled simply by varying input power to each motor as shown in Figure 7. This reduces the number of moving parts to essentially just the four motors/rotors, with the potential for cost savings and reliability. Another benefit to the quadrotor is its popularity amongst the hobbyist community which presents a wealth of resources for constructing a proof-of-concept (POC) aircraft.

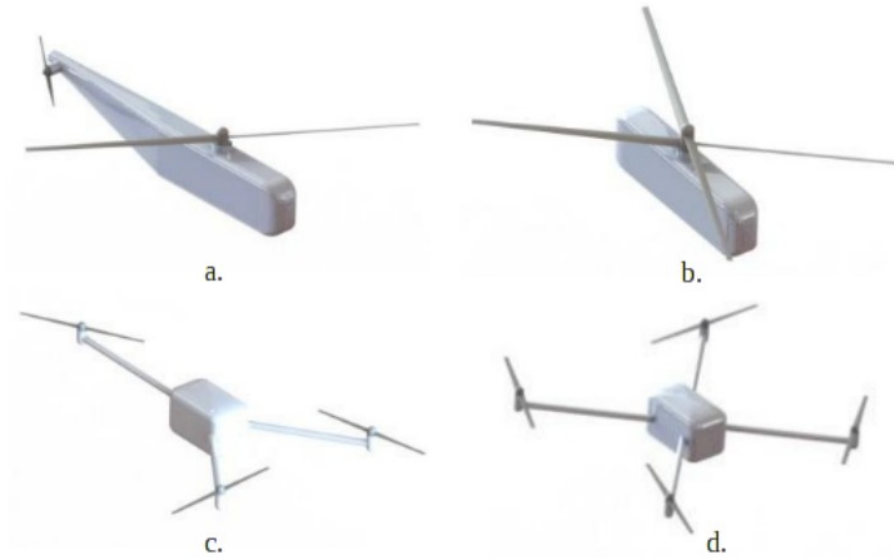


Figure 6a-d: Possible rotorcraft configurations: a Conventional Helicopter, b. Coaxial, c. Trirotor 'Y', d. Quadrotor

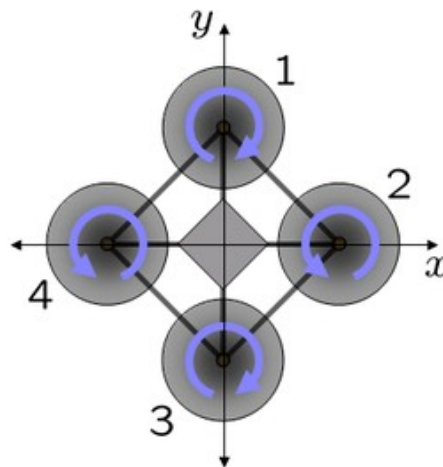


Figure 7: : Fundamental control of a quadrotor. With each rotor rotating in these specified directions, the net yaw torque on the vehicle is null. [15]

It is also worthy of mentioning that lighter-than-air vehicles including small airships and balloons are also capable of carrying the relay payload but do not meet all the outlined requirements. The airship will need to be inflated at launch with a certain gas and is tactically poor due to its low maneuverability and high profile. A balloon must be tethered, which easily gives away the sender's location. Both lighter-than-air vehicles perform very poorly in inclement weather in which it cannot maintain station-keeping.

2.2 VEHICLE SIZING AND PACKAGING/STOWING

To comply with the size restrictions of most backpacks, the largest dimension of the platform in packed configuration must be no greater than 18 inches. The first step in increasing the aircraft's compactness in packed configuration is to utilize folding components. Figure 8 shows a quadrotor with each of the four arms rotated inwards 45 degrees and the 18" size restriction, with Figure 9 being prior to folding.

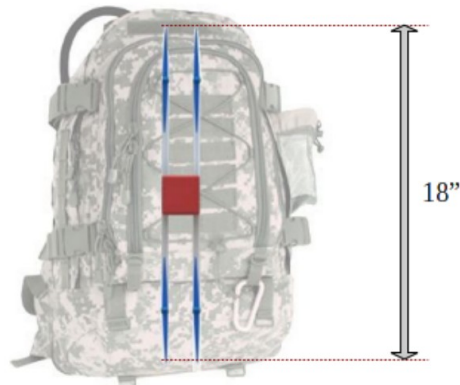


Figure 8: Folded quadrotor inside the 18in length restriction.

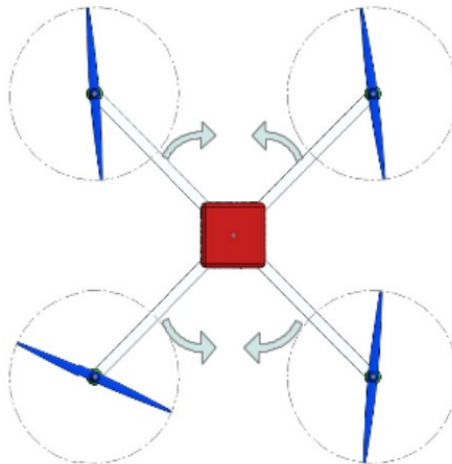


Figure 9: Quadrotor prior to folding in flight-ready configuration. Arms rotate inwards 45 degrees.

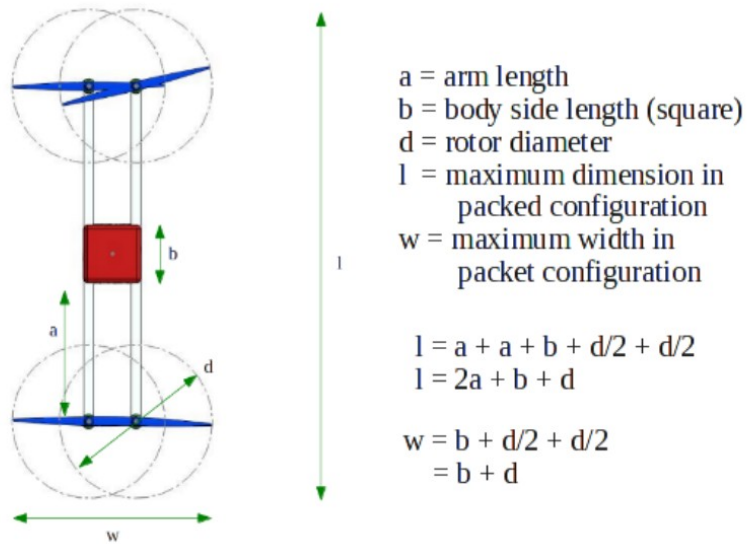


Figure 10: Quadrotor dimensions in packed configuration.

Figure 10 shows representative dimensions of each major component and the extrapolated lengths in packed configuration. Note that l and w are defined for 'worse case' scenarios when the rotors are oriented such that they maximize l or w . When all the rotors are oriented 90 degrees to the arms as shown and w is maximized, l will not be as large as defined above but rather: $l = 2a + b$. It will be noted in detail in following sections that the rotor diameter must be maximized within the dimensional restrictions for greater hover efficiency. Figure 11 describes the condition such that the rotor blades do not intersect when flying.

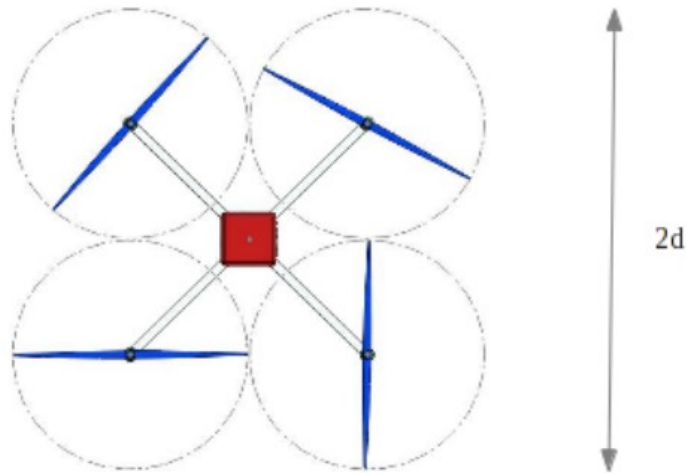


Figure 11: Maximum diameter rotors. The rotor disk [diameter] is marked by the gray hatched circles.

When the rotor diameter d is maximized without rotor intersection as shown in Figure 10 and adhering to the condition for l in Figure 8 and $b = 3''$ (average relay dimension), these arguments are derived:

$$2(a + \sqrt{(9/2)})^2 = d^2 \quad (1)$$

$$18 = 2a + 3 + d \quad (2)$$

Solving simultaneously yields $a = 3.5$ inches and $d = 8$ inches. If all the rotors are allowed to be cocked 90 degrees when packed as in Figure 10, then $w = 11$ inches and $l = 10$ inches. This approach allows a maximum dimension less than the allowable 18 inches, but requires almost twice the area inside the backpack/container. An additional method for folding the airframe is to hinge the arms inwards towards the base as shown in Figure 12.

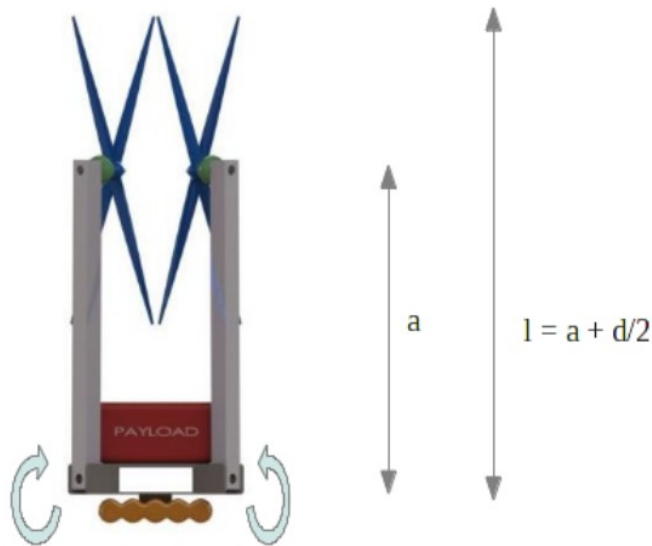


Figure 12: Arms rotate upwards and inwards as illustrated. The relay/payload is shown in red and batteries in orange.

Following the previous procedure with the method in Figure 11:

$$18 = a + d/2 \quad (3)$$

which yields $a = 9.6$ inches and $d = 16.8$ inches. This folding method allows for the largest possible diameter while also consuming the least amount of space while packed.

2.3 WEIGHT ESTIMATE

Table 1 summarizes weight estimates for the aircraft, its components, and payload (TCCR). Many of the listed hardware weights are from comparable hobbyist components.

Table 1: Weight estimates.

Component	Weight (g)	Quantity	Net Weight (g)	% Of Total
Frame	312	1	312	21.2
Motor	72	4	288	19.6
ESC	21	4	84	5.7
APM Board (Control)	45	1	45	3.1
Rotor	12	4	48	3.3
Payload	454	1	454	30.9
Batteries (2200mAh)	190	1	190	12.9
Misc. Hardware	50	1	50	3.4
		TOTAL	1471	
			14.5N	

The 2200mAh battery noted provides a relatively high energy density and is commonly used for small aircraft applications. All else being constant, adding additional battery packs in parallel will indeed increase the endurance but also increases the weight - requiring more thrust and thus more power to hover. The frame weight is based on an off-the-shelf aluminum hobbyist quadrotor frame shown in Image 3a-b. Utilizing much lighter carbon composite frame materials has the potential to significantly reduce the airframe's total weight and increase endurance.

2.4 HOVER POWER ESTIMATE

The momentum theory is used to obtain preliminary estimates for rotorcraft performance in hover and climb. In short, the momentum theory is derived from the balance of mass, momentum, and energy through an actuator disk. However, this model does make some underlying assumptions that produce and underestimate for power required, namely: the flow is incompressible, steady, inviscid, irrotational, uniform, one-dimensional, and that there is no swirl in the rotor's wake or tip losses. [7] The derived form for this estimate of power to hover, known as ideal power, is given by:

$$P_{ideal} = T * \sqrt{\left(\frac{T}{2 * \rho * A}\right)} \quad (4)$$

where T is the thrust, rho is the air density, and A is the rotor's disk area (circle of diameter d). For the quadrotor configuration in [unaccelerated] hover:

$$W = \sum T = 4T \quad (5)$$

With the above equation for ideal power and the net weight estimate, a MATLAB program was written to plot ideal power as a function of rotor diameter. Figure 13 is the resulting plot showing the total ideal power to hover for all four rotors as a function of disk area. Utilizing the latter folding method in the previous section with its 16.8 inch rotor diameter, the total ideal power is approximately 45 Watts.

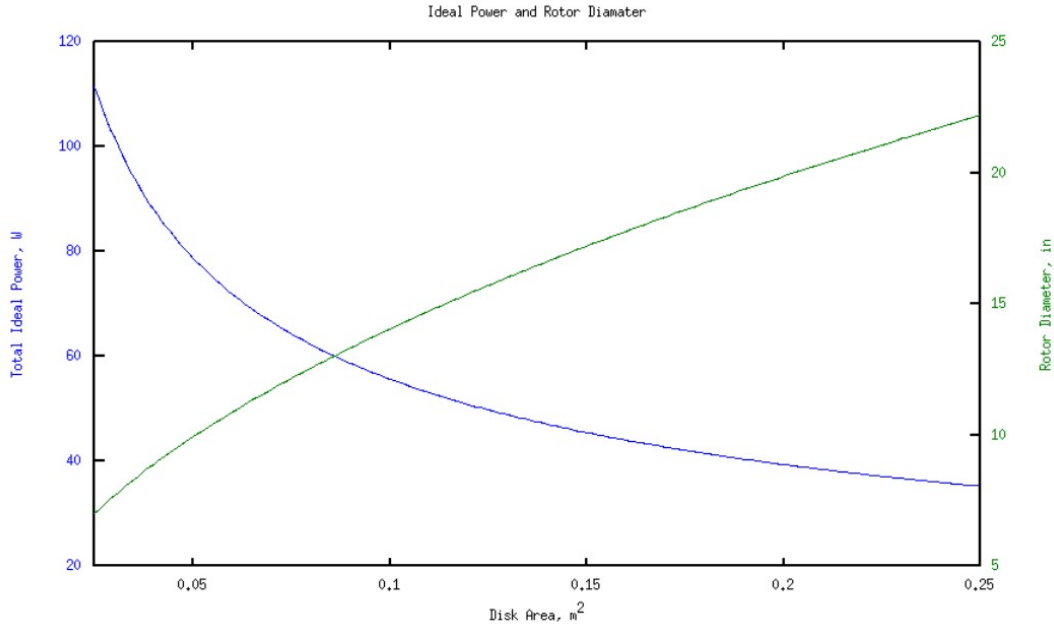


Figure 13: MATLAB plot for total ideal power from momentum theory.

2.5 ENDURANCE ESTIMATE

An estimate for the aircraft's flight endurance [in hover] is estimated from the ideal power and the average consumption by components. The efficiency of the electronic speed controllers (ESC) and motors are average values for similar hobby products. Figure 14 graphically depicts the distribution of power from the battery to the all the respective components. Solving for the amperage draw for each component from the 2200mAh source yields a hover endurance of 21 minutes. Several voltage step-ups and step-downs are required at each junction to modify the battery's 11.25 V input voltage and are not included. The absence of these deceives with their own efficiency factors leaves the solution a slight overestimate.

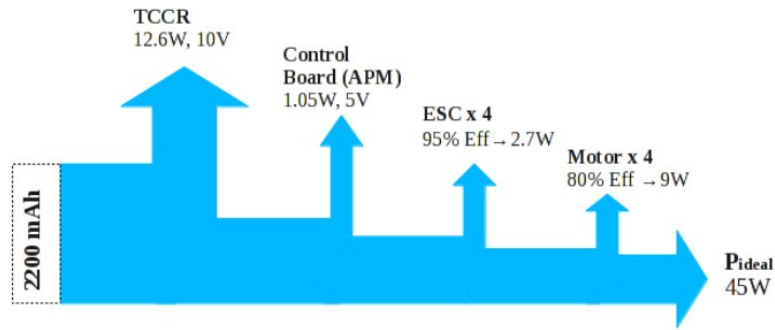


Figure 14: Power distribution for platform and components.

It may be presumed that to increase the flight endurance the number and/or capacity of batteries should simply be increased. Doing so, however, increases the weight and thus thrust required to maintain hover. Producing more thrust with given hardware accordingly increases the power consumption. A MATLAB program was written that incorporates the optimum rotor diameter of 16.8 inches and the ideal power to hover the aircraft with increasing the battery capacity to determine its resulting endurance. Figure 15 represents the hover endurance as a function of battery capacity. Note the trend of diminishing returns.

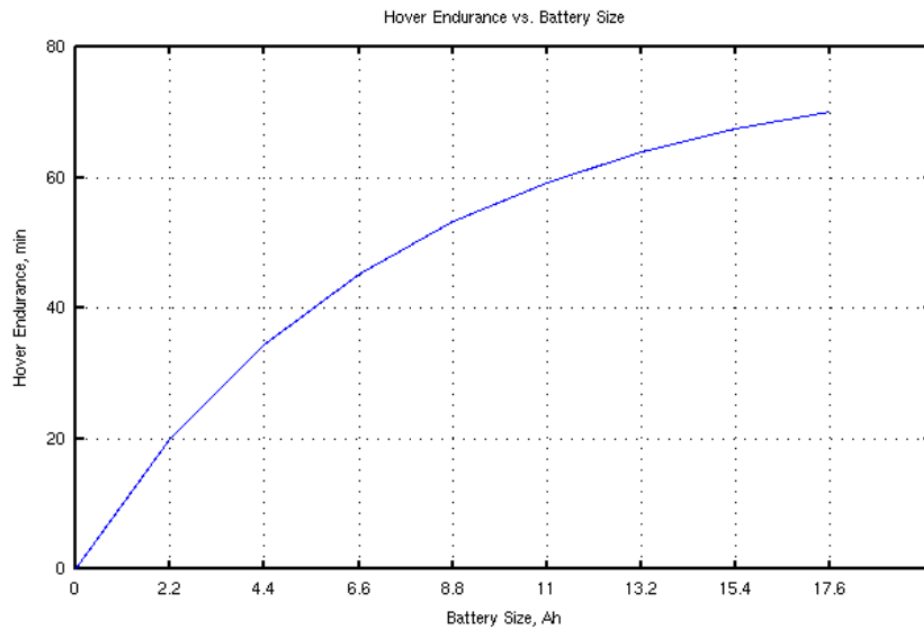


Figure 15: Hover endurance vs. battery capacity. Each tick along the abscissa is one 2200mAh battery.

3.0 PROOF-OF-CONCEPT (POC) DEVELOPMENT

A POC aircraft is being constructed in parallel using primarily hobbyist components. The goals with the POC are as follows:

- Test and validate rotors developed for the theoretical design
- Integrate and test the off-the-shelf control system
- Technology demonstration purposes

Two key components have been obtained: The ArduPilot 2.0 comprehensive control board and a folding quadrotor frame (Image 2a and 2b).

The ArduPilot Mega 2.0 (APM2) includes the following capabilities [11]:

- Arduino Compatibility
- Plenty I/O straight pins for sensor/motor connectivity
- Digital compass
- GPS
- Programmable autopilot
- 6-DOF accelerometer and gyros
- Barometric pressure sensor/altimeter
- PC-based API



Image 2a: Flight-ready Configuration.



Image 2b: Collapsed Configuration.

One of the greatest benefits this device offers to the project is hardware flexibility. The APM2 delivers a dependable and compatible electronic platform on which to build upon. All stability and control hardware and software is already included and will require minimal configuration, as that aspect is not in this project's scope. Once motors have been chosen, they along with their requisite motor controllers could be connected to the APM2. Of course some configuration and calibration will be required before safe and successful flight operations. Image 3 is a screenshot of the APM2's API showing live data feeds from the board. Clockwise from the right side are attitude indicator, geographic location and heading, and a graph showing live pitch, roll, and yaw angles. Once the hardware is integrated with the APM2, simple instructions in Arduino could command the aircraft to hover as the minimum design objectives specify. Once the aircraft could reliably and safely hover at 50 feet it will be outfitted with a compact Wi-Fi router as shown in Figure 16. The router will enable the system to perform a demonstration whereas the aircraft will hover at some 50 feet and allow two laptop computers that are otherwise out of line-of-sight and/or range to successfully transmit data. Because Wi-Fi has a relatively high dissipation rate and data transmissions could be explicitly verified gives this demonstration great impact.



Image 3: Screenshot of live flight data from the APM2 board showing attitude, geographic location, and roll/pitch rates.

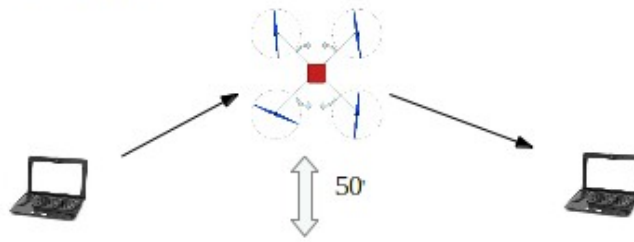


Figure 16: Initial mission for POC aircraft.

Unfortunately, other than general COTS and open-source software and hardware familiarization, not much progress was made with respect to proof-of-concept vehicle test article development. However, the background research did lead to, first, a clarification of the technical challenges of sizing the vehicle and the necessity of improving the conceptual vehicle's hover efficiency and endurance and, second, the acquisition and development of single rotor test articles for the experimental work conducted as a part of this study.

4.0 CHALLENGES IN IMPROVING VEHICLE HOVER EFFICIENCY AND ENDURANCE

The proof-of-concept work performed to date was overall quite promising but it is still clear that substantial improvements to vehicle hover efficiency and endurance need to be made for quadcopter configurations to achieve the size, weight, and payload requirements associated with the LOS communication relay mission. Chief among the challenges implicit in improving quadcopter efficiency and performance is those related to rotor design and operation in low-Reynolds aerodynamic regimes. This section of the report will provide background information into airfoil and rotor aerodynamics while operating a low-Reynolds numbers.

4.1 AIRFOILS AND ROTORS OPERATING IN THE LOW REYNOLDS NUMBER REGIME

The low Reynolds numbers that aircraft of this size, weight, and speed operate in poses an additional technical challenge. Whereas the generic passenger-carrying aircraft operates in Reynolds numbers greater than 100000, aircraft such as the quad rotor experience Reynolds number of 10000 and less. Because of the focus in larger [transport] aircraft during the last century, there is relatively little research in the area of low Reynolds number flight. Figure 17 illustrates the vast range of Reynolds numbers.

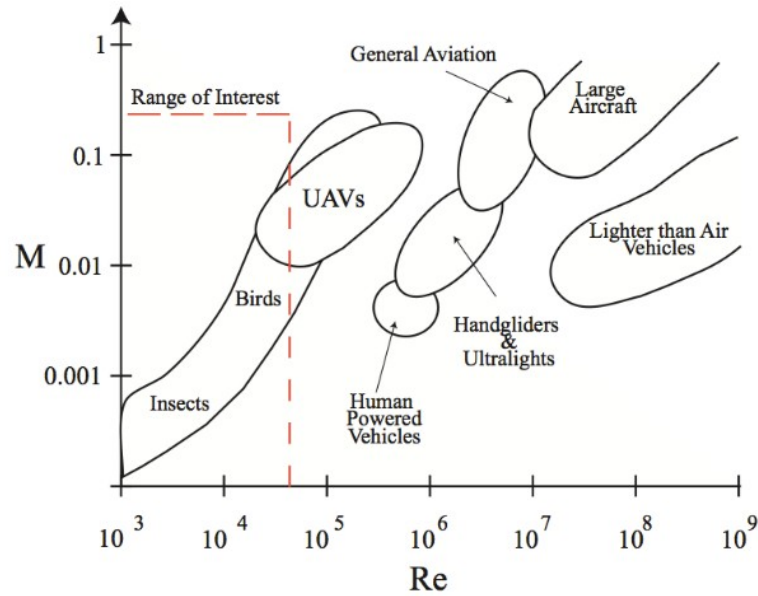


Figure 17: Reynolds number ranges for various flight vehicles. [7]

The rotor of a rotorcraft is a particularly critical component as it is responsible for both lift generation and propulsion. Part of preliminary rotor design involves optimizing airfoil sections along the rotor's span for the particular flight conditions experienced at that section. At a constant rotational velocity, local incident velocity that a rotor element experiences is a function of its respective radius as illustrated in Figure 18.

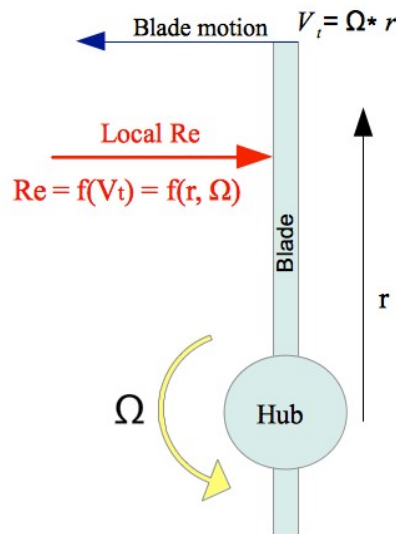


Figure 18: Local Reynolds number as a function of radial location.

A small routine was written in MATLAB to calculate the Reynolds number experienced at radial locations along the blade of the 16.8" diameter rotor for various RPMs. Figure 2 shows

the script's output. The motors of the current prototype have a rotational output capacity of 880 kV (RPM per input Volt). With the 11.1 V max output battery the rotor could potentially rotate at almost 10000 RPM, although such speeds will only occur during heavy maneuvering or climb. Exact angular velocities in hover are not yet known, but it is estimated that the rotors will spin at approximately 1000-3000 RPM for steady level flight. Note from Figure 19 that the inner portions of the rotor encounter Reynolds of less than 10000 at 2000 RPM.

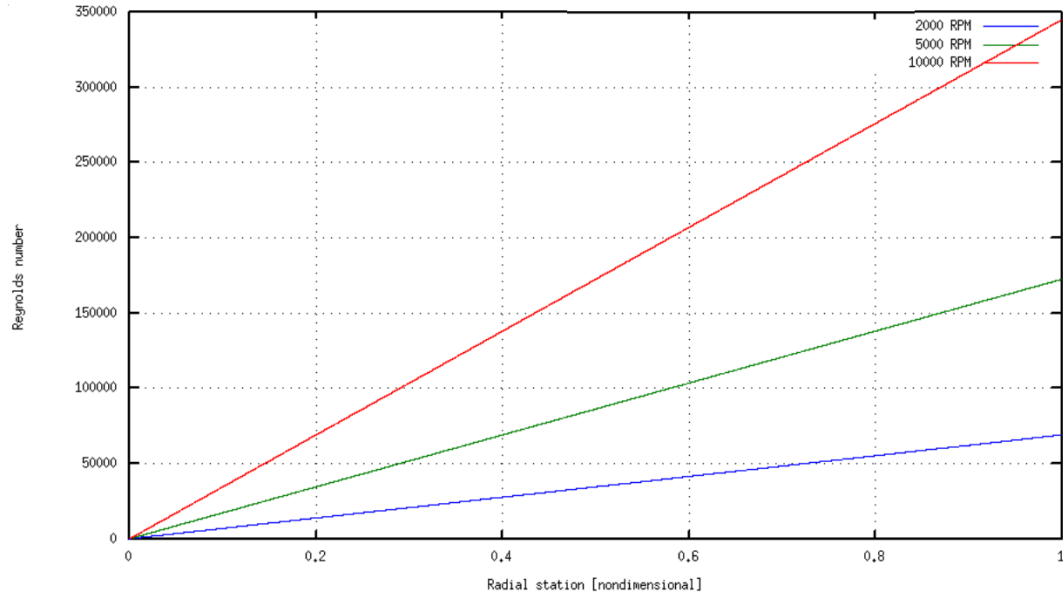


Figure 19: Reynolds number vs. radial location for 2000, 5000, and 10000 RPM.

4.2 BOUNDARY LAYERS ON AIRFOILS

The boundary layer has a considerable affect on performance and drag at low Reynolds numbers. By definition, Reynolds number is the ratio of inertial to viscous forces of a fluid on a wall. At low Reynolds numbers the viscous forces dominate the total drag force exerted on the body. The viscosity causes a thin layer of air to “stick” the surface, also known as the no-slip condition. From this non-moving layer at the wall up to 99% of the free stream velocity encompasses the total thickness of the boundary layer. There are two primary classifications of boundary layer states; laminar and turbulent. Uniform and continuous flow comprises laminar boundary layers whereas disorderly, mixing, and an overall thicker flow profile defines turbulent boundary layers. Also inherent to turbulent boundary layers are a significantly greater coefficient of drag. When free stream air initially encounters the wall in consideration the until the flow is perturbed and the boundary layer transitions from laminar to turbulent. An overall greater total drag could be caused by an earlier than desired transition from laminar to turbulent and a longer wetted surface under the turbulent boundary layer.

One major influence of boundary layer transition is the stream-wise gradient of local pressure. An increase of pressure with the flow, in accordance with Bernoulli's principle, coincides with a decrease of local free stream velocity and an expansion of the boundary layer

profile. This stream-wise increase in pressure is known as an adverse pressure gradient. Conversely, a favorable pressure gradient is a decrease in stream-wise pressure resulting in an increase in local velocity that maintains the laminar profile of the boundary layer. These two scenarios are illustrated in Figure 20 a) and b).

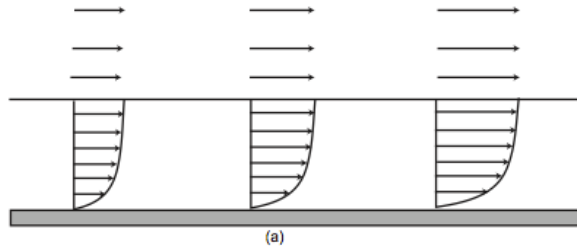


Figure 20a: Laminar boundary layer. [7]

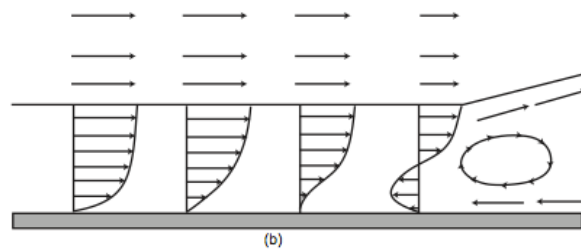
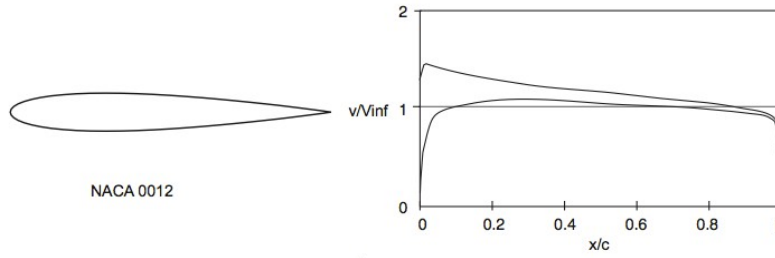


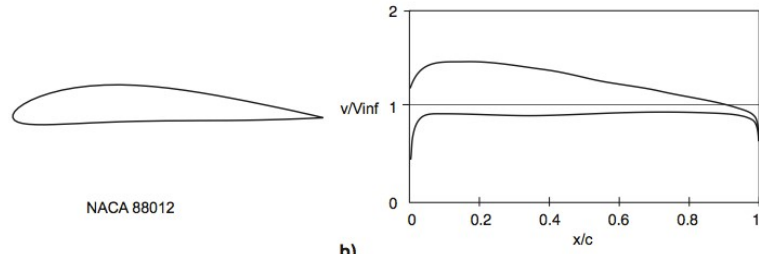
Figure 20b: Transitional boundary layer. [7]

When an adverse pressure gradient adequately perturbs a laminar boundary layer it will either separate and reattach as a fully turbulent boundary layer, separate and stall the airfoil/blade, or immediately transition into a turbulent boundary layer. The stream-wise curvature of the particular wall is a fundamental source of pressure gradients. The affect of transition and separation, whether due to airfoil curvature or angle of attack, could be mitigated by the use of thin cambered airfoils. Figures 21a-c show three airfoil profiles and their respective velocity distributions over the upper and lower surfaces in inviscid flow at 3 degrees angle of attack. Note the relatively slower velocity distribution on the lower surface of the cambered NACA 6406. This deceleration and accompanying higher pressure at the lower surface allows the airfoil to continue to produce lift when the flow on the upper surface may be separated and stalled.



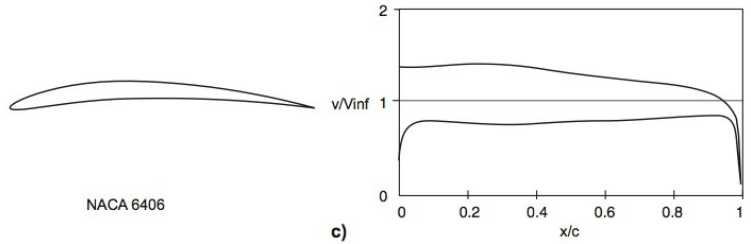
a)

Figure 21a: Velocity distributions over NACA 0012 airfoil. [7]



b)

Figure 21b: Velocity distributions over NACA 88012 airfoil. [7]



c)

Figure 21c: Velocity distributions over NACA 6406 airfoil [7].

4.3 LAMINAR SERARATION BUBBLE

At the point of transition from a laminar to turbulent boundary layer there exists a small region of recirculating flow at the wall. This is known as the laminar separation bubble and is illustrated in Figure 22.

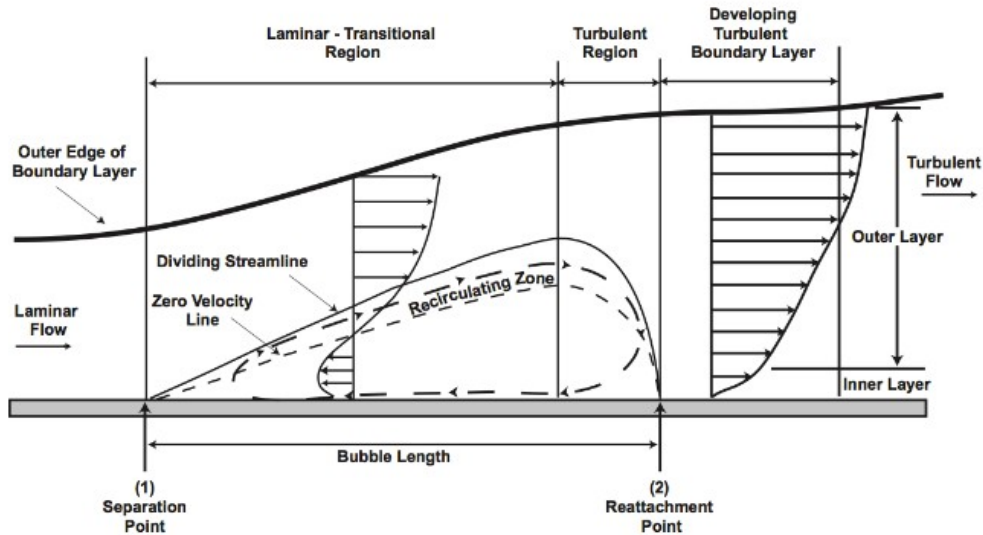


Figure 22: Transitional boundary layer showing separation bubble and turbulent reattachment. [7]

Within this bubble the lower portion of the flow is reversed and physically undergoes a transformation from laminar to turbulent flow. The downstream portion of the bubble contains fully turbulent flow. These bubbles are known to appear at Reynolds numbers from 30,000 to 70,000. Referring to Figure 18, this range of Reynolds numbers would exist at the outer portion of the rotor at the highest rotational velocities. At Reynolds numbers below this range, laminar boundary layers separate without the occurrence of a bubble. Laminar separation bubbles also cause streamlined airfoils to exhibit hysteresis with small variations in angle of attack and Reynolds number. The Reynolds number at which transition occurs is known as the critical Reynolds number and differs for each airfoil.

4.4 AIRFOIL BEHAVIOR

Research performed by Schmitz [7] has concluded that there is a significant performance penalty for traditional streamlined airfoils when they are operated below their critical Reynolds number. Schmitz also discovered that flat plates and cambered airfoils do not exhibit hysteresis as do streamlined airfoils. Five distinct airfoils tested by Schmitz are shown in Figure 23. A plot of C_{l_max} for these airfoils over a range of Reynolds numbers is shown in Figure 24.

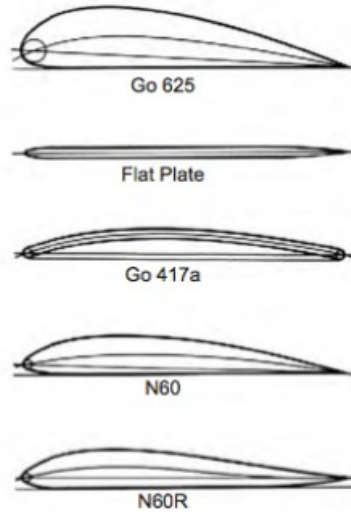


Figure 23: Five airfoils examined by Schmitz. [7]

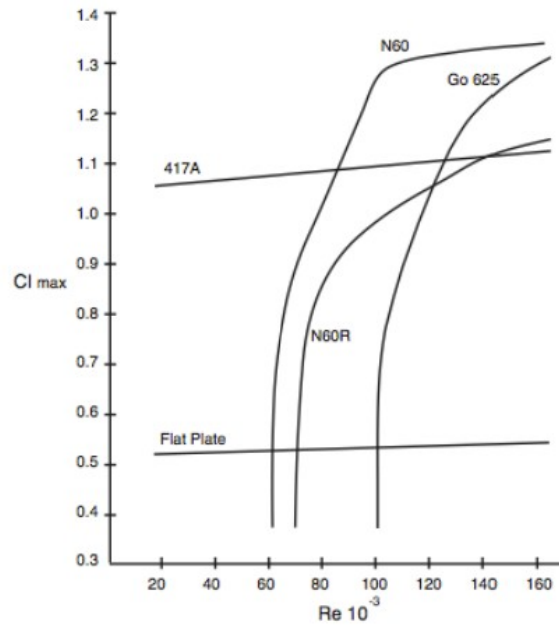


Figure 24: $C_{l\ max}$ vs. Reynolds number for the five airfoils examined by Schmitz. [7]

Note that although the streamlined N60 and Go 625 airfoils have greater performance in terms of $C_{l\ max}$ than the other airfoils at Reynolds numbers above 100,000, the C_l of the flat plate and Go 417a does not dramatically fall as Reynolds number decreases below 100,000. Although they do not have the C_l potential of the streamlined airfoils, the flat plate and Go 417a have a linear and predictable C_l slope as Reynolds number increases. Figure 25 shows Schmitz's results for minimum coefficient of drag for the set of five airfoils. The streamlined Go 625 and N60 airfoils produce significantly more drag when operating below their optimum range of Reynolds numbers.

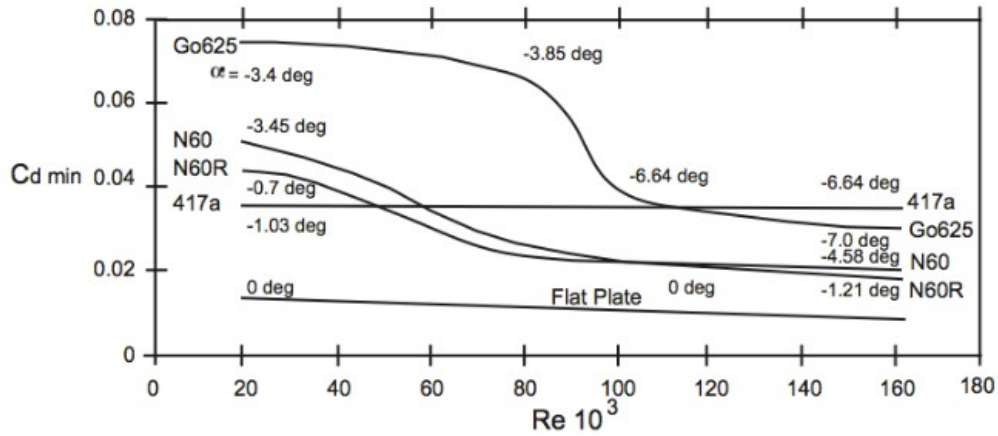


Figure 25: Minimum coefficient of drag vs. Reynolds for Schmitz's five airfoils. [7]

Continuing the research into low Reynolds number aerodynamics, Laitone[7] discovered that the performance of flat and cambered plates could be further improved by implementing sharp leading edges. The sharp leading edges induce small vortices on the upper surface of the airfoil that prevents separation. Laitone also showed that at low Reynolds numbers the Kutta condition at the airfoil's trailing edge is not necessary for lift generation. Figures 26a) and b) summarize Laitone's research into sharp leading edges and flat/cambered plates, respectively.

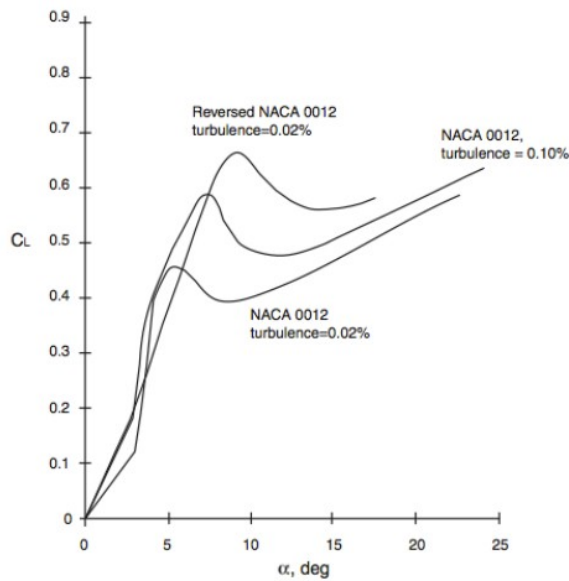


Figure 26a: Coefficient of lift vs. angle of attack for NACA 0012 with varying turbulence and orientation. [7]

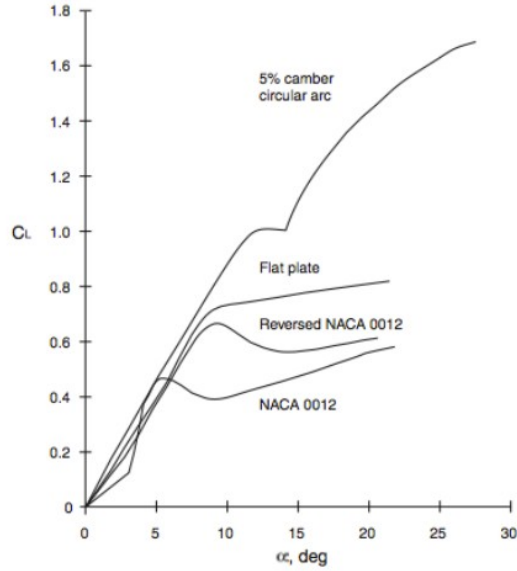


Figure 26b: Coefficient of lift vs. angle of attack for NACA 0012, flat plate, and cambered plate. [7]

McMasters and Henderson [7] further complimented Laitons's and Schmitz's research into very low Reynolds number flight. This work is shown in Figures 27 and 28 shows the same coefficient of lift decline at low Reynolds numbers as Figure 24 and includes coefficient of lift data for insects.

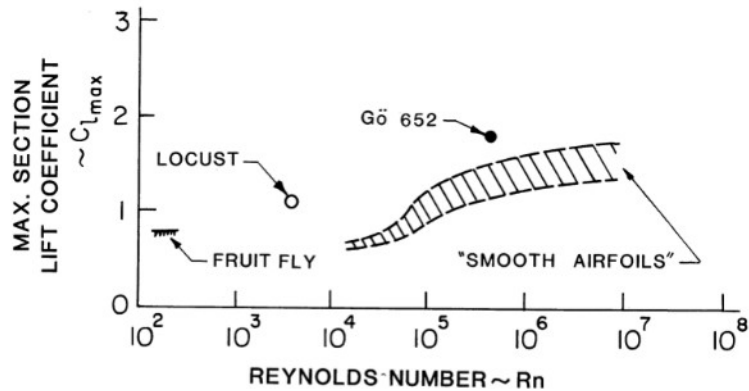


Figure 27: Compilation of lift coefficients at increasing Reynolds numbers.

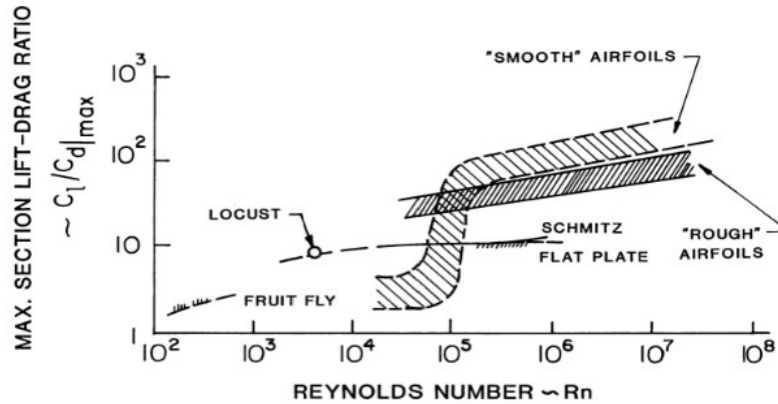


Figure 28: C_l/C_d_{max} for various flight bodies over increasing Reynolds numbers.

5.0 ROTOR AERODYNAMICS AND HOVER PERFORMANCE

5.1 BLADE ELEMENT THEORY

Momentum theory provides a reasonable estimate for the power required to hover and rotor diameter, but does not, in itself, provide any specific insights into the rotor's geometry including the number of blades, airfoil characteristics, and planform required for optimal performance. The next step in rotor design involves determining the proper airfoil section and typically utilizes the blade element theory. In Blade Element Theory, the lift and drag characteristics are analyzed at infinitesimally thin airfoil sections along the rotor blade and then integrated from the rotor's root to tip to obtain total thrust and power consumed. This is illustrated in Figure 29, where b is the number of blades. The rotors hub and blade joints take up a small yet significant diameter that does not generate lift and is known as the root cut out area. Elemental thrust and power are integrated over the blade's span to yield total thrust and power as expressed in equations 6 and 7, respectively. [8]

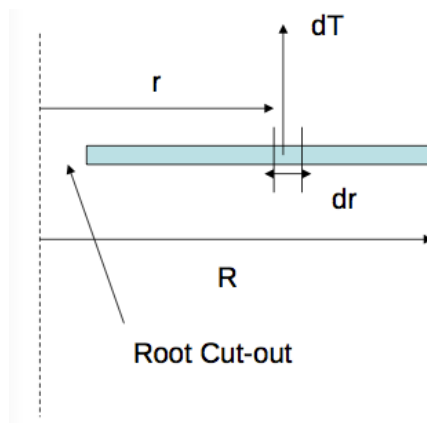


Figure 29: Elemental rotor sections. [8]

$$T = b \int_{\text{Cut-Out}}^{\text{Tip}} dT \quad (6)$$

$$P = b \int_{\text{Cut-Out}}^{\text{Tip}} dP \quad (7)$$

An infinitesimal airfoil section, its pitch angle, and induced velocity are sketched in Figure 30. Equations 8 and 9 resolve the induced angle of attack and effective angle of attack, respectively.

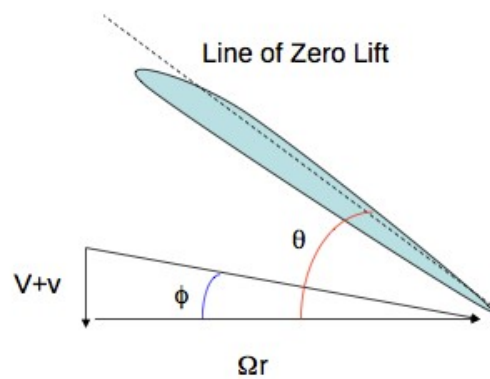


Figure 30: Inflow velocity, pitch angle, and inflow angle angle of attack. [8]

$$\phi = \arctan\left(\frac{V + v}{\Omega r}\right) \quad (8)$$

$$\alpha_{\text{effective}} = \theta - \phi \quad (9)$$

With the effective angle of attack at each airfoil station, sectional lift and drag values are computed from airfoil properties provided by data tables. The expressions for sectional lift and drag are expressed in Equations 10 and 11, respectively, where U_t is the tangential velocity from rotation and U_p is the inflow velocity.

$$\Delta L = \frac{1}{2} \rho (U_t^2 + U_p^2) c C_l \quad (10)$$

$$\Delta D = \frac{1}{2} \rho (U_t^2 + U_p^2) c C_d \quad (11)$$

From the section lift and drag expressions, sectional expressions for thrust, axial force and power are derived in Equations 12, 13, and 14, respectively. [8]

$$\begin{aligned} dT &= (\Delta L \cos(\phi) - \Delta D \sin(\phi)) dr \\ &= \frac{1}{2} \rho (U_t^2 + U_p^2) c (C_l \cos(\phi) - C_d \sin(\phi)) dr \end{aligned} \quad (12)$$

$$\begin{aligned} dF_x &= (\Delta D \cos(\phi) + \Delta L \sin(\phi)) dr \\ &= \frac{1}{2} \rho (U_t^2 + U_p^2) c (C_d \cos(\phi) + C_l \sin(\phi)) dr \end{aligned} \quad (13)$$

$$dP = U_t dF_x = \Omega r dF_x \quad (14)$$

5.2 BLADE ELEMENT MOMENTUM (BEM) THEORY

Although more physically accurate than momentum theory and appropriate for detailed fixed-wing analysis, blade element theory has drawbacks when applied to helicopter rotors. Blade element theory does not account for tip losses, swirl wake losses, and assumes that the inflow velocity to the rotor is uniform, leading to an underestimate of power required. The BEM method incorporates the same numerical procedure as the blade element theory but also includes terms for the non-uniform flow. In BEM, the rotor disk is divided into a thin annulus as shown in Figure 31. The area of the annulus, mass flow rate through the annulus, and thrust created by the annulus is calculated in Equations 15, 16, and 17, respectively. [8]

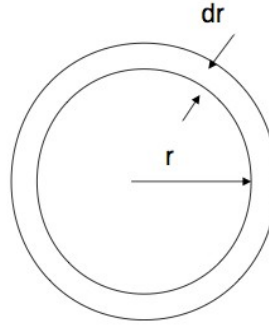


Figure 31: Elemental annulus in BEM theory. [8]

$$\text{Area} = 2\pi r dr \quad (15)$$

$$\text{Mass flow rate} = 2\pi r \rho (V+v) dr \quad (16)$$

$$dT = 4\pi r \rho (V+v) v dr \quad (17)$$

The differential thrust for the annulus incorporating sectional airfoil geometry is expressed in Equation 19, where a is the lift slope, b is the number of blades and c is the blade chord.

$$\begin{aligned} dT &= b \cdot \frac{1}{2} \rho \cdot (\Omega r)^2 c \cdot C_l \cdot dr \\ &= abc \cdot \frac{1}{2} \rho \cdot (\Omega r)^2 \cdot \left(\theta - \frac{V+v}{\Omega r} \right) \cdot dr \end{aligned} \quad (18)$$

5.3 BEM ROTOR ANALYSIS

A MATLAB routine [10] performs the BEM numerical procedure based on the airfoil sections lift slope, coefficient of drag, rotor size, and angular velocity. The BEM MATLAB routine was carried out for a completely flat plate rotor, a rotor consisting completely of a NACA 2412 airfoil, three hybrid rotors where the transition point from flat plate to 2412 varies radially. The rotor diameter used is 16.8” (calculated from prior momentum theory) and a median pitch of 4.7 degrees. Figure 32 shows the resulting output for rotor thrust as a function of increasing RPM.

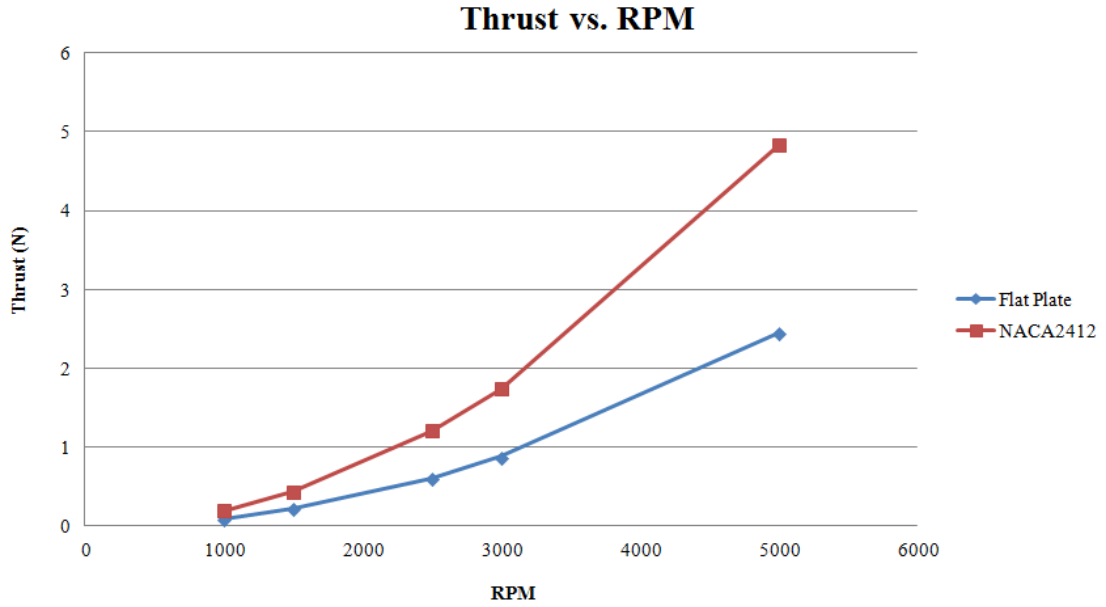


Figure 32: Thrust vs. RPM for flat plate and NACA 2412 from BEM.

Figure 33 represents the power required to maintain a constant rotational velocity and the resulting thrust produced by the flat plate and NACA 2412 rotors.

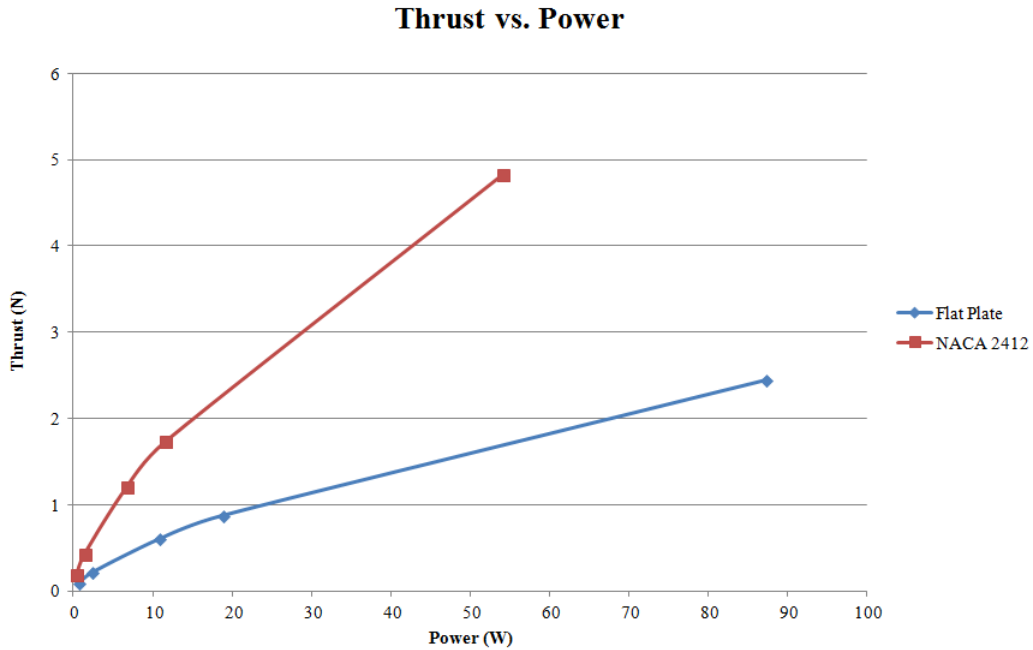


Figure 33: Power vs. RPM for flat plate and NACA 2412 from BEM.

Figure 34 shows the resulting thrust and power required for the hybrid rotor as the location of transition from flat plate to NACA 2412 airfoil is moved radially towards the rotor tip.

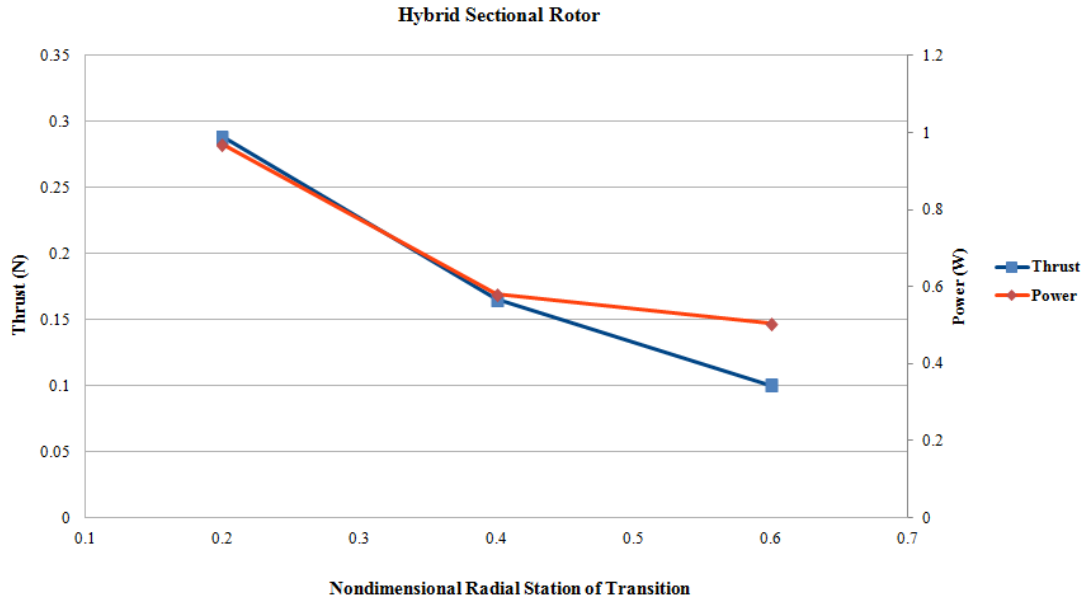


Figure 34: Thrust vs. radial location of geometric transition.

From these results from the BEM analysis, it could be concluded that:

- Below 2000 RPM where according to Figure 2 the blades Reynolds number is mostly below 50000, the flat plate rotor produces slightly more thrust than the 2412 airfoil rotor.
- Given that the total estimated weight of the aircraft is 14.5 N and the thrust results are per each of the four rotors, the angular velocity needed to hover need not exceed 3500 RPM
- At angular velocities above 5000 RPM, the flat plate rotor consumes significantly more power than the 2412 rotor
- At 1500 RPM (low Re), it is advantageous to move the transition point outboard towards the rotor tip.

6.0 ROTOR CFD ANALYSIS

Computational Fluid Dynamics (CFD) was utilized to further investigate the performance of the rotors at low Reynolds numbers at a higher level of fidelity. CFD allows the effects of viscosity and separation to be accounted for in estimating the performance of the rotor blade design. Two different rotor blades are considered: one “standard” blade consisting of a NACA 2412 streamlined airfoil throughout the span, and a “hybrid” blade with a Goe 417a cambered plate airfoil from the hub to 40% of the span and a NACA 2412 throughout the remaining outboard section. Both blades do not incorporate taper or twist, and are set at a constant 4.7 degrees pitch throughout the span.

6.1 APPROACH

To best resolve the low Reynolds number conditions, the pressure-based CFD-ACE+ code was used in conjunction with the low-Re Two-Layer k- ϵ Chien turbulence model in steady state. This turbulence model provides a more accurate representation of low Reynolds number physics near the wall than does the standard k- ϵ model and wall functions. Another benefit to the low-Re Chien model is that it does not require extremely fine grid resolution at the wall, which alleviates some of the computational expense. In this model, the cell zone near the wall is divided into two sublayers. The sublayer directly adjacent to the wall where viscosity is dominant uses a one-equation model where the ϵ variable is replaced by an algebraic relation. The sublayer away from the wall is resolved with the standard k- ϵ model commonly used at higher Reynolds numbers. Turbulent viscosity and damping function for the model are calculated by Equations 19 and 20, respectively. [9]

$$\mu_t = C_\mu f_\mu \frac{\rho k^2}{\epsilon} \quad (19)$$

$$f_\mu = \frac{l_\mu}{l_\epsilon} \quad (20)$$

Length scales for the turbulence variable are defined by Equations 21 and 22 and local turbulence Reynolds number expressed by Equation 23. [9]

$$l_\mu = C_\mu y \left[1 - \exp\left(-\frac{Re_k}{a}\right) \right] \quad (21)$$

$$l_\varepsilon = \frac{C_y y}{1 + b/Re_k} \quad (22)$$

$$Re_k = \frac{\sqrt{k} y}{\nu} \quad (23)$$

The constants for the model are $a=50.5$, $b=5.3$, and $C_1 = kC_\mu^{-3/4}$. The location of the sublayer interface is where the damping function is equal to 1. Below this value, the dissipation rate is calculated by Equation 24. [9]

$$\varepsilon = \frac{k^{2/3}}{l_\varepsilon} \quad (24)$$

A three dimensional C-type fully structured grid was created for a single blade for each of the two geometries. The grid resolution was 75x150x75 grid points and is shown in Figures 35-37.

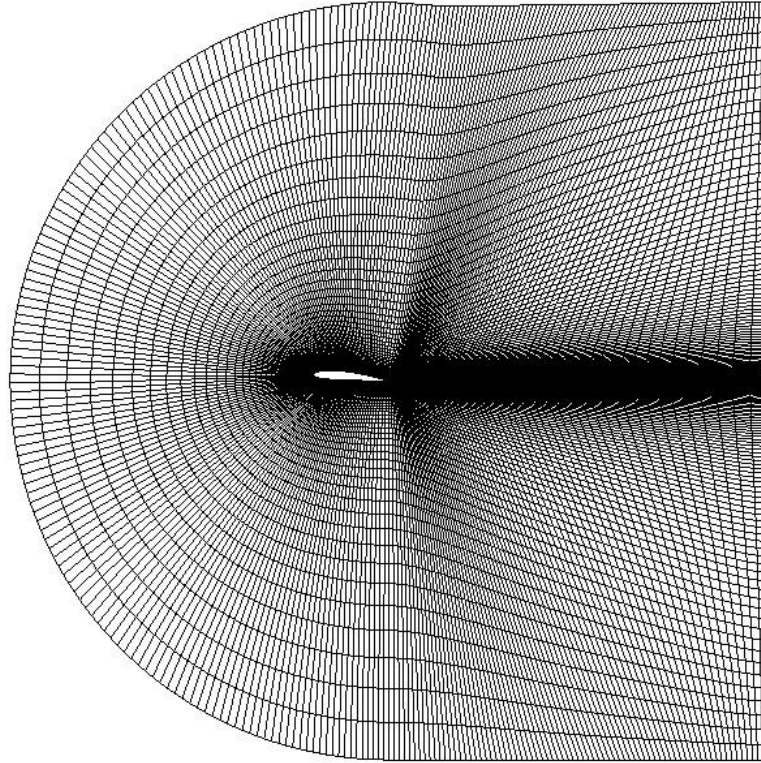


Figure 35: Structured grid around standard rotor.

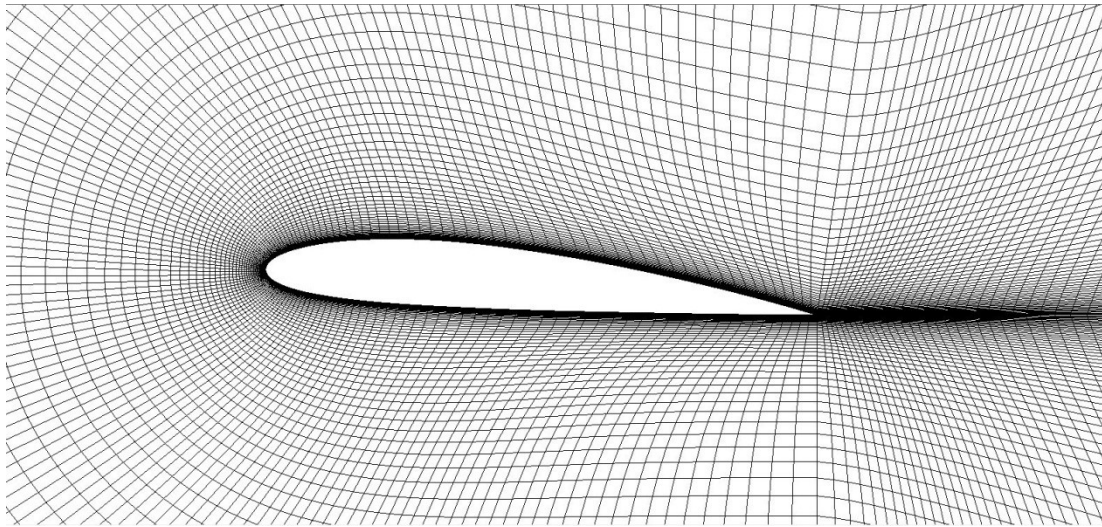


Figure 36: Structured grid around NACA 2412 section.

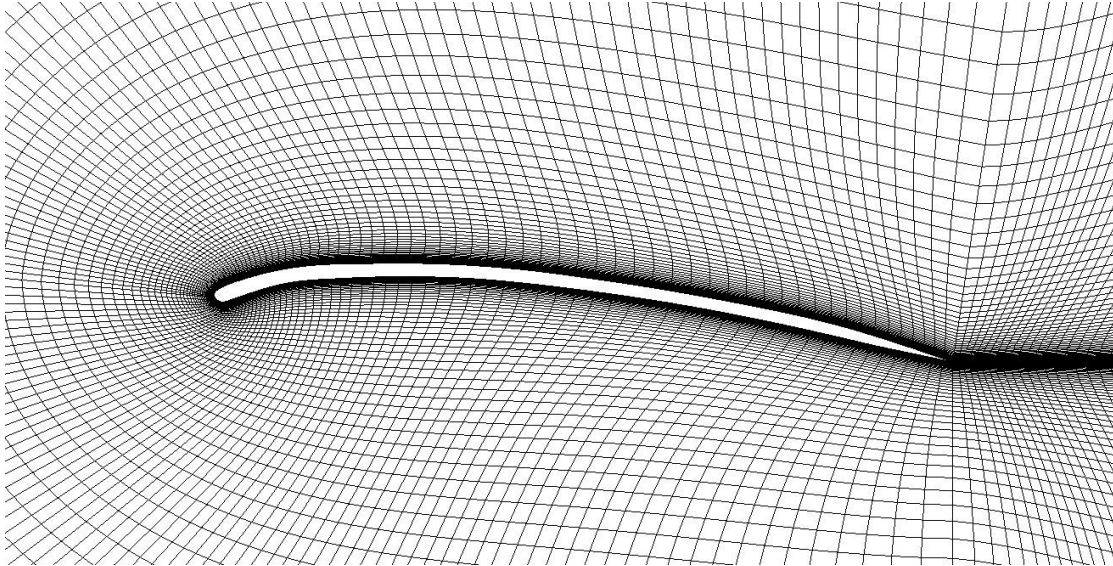


Figure 37: Structured grid around Goe 417a section.

An interpolative loft between the Go 417a and NACA 2412 at 40% span was created and is shown in Figure 38.

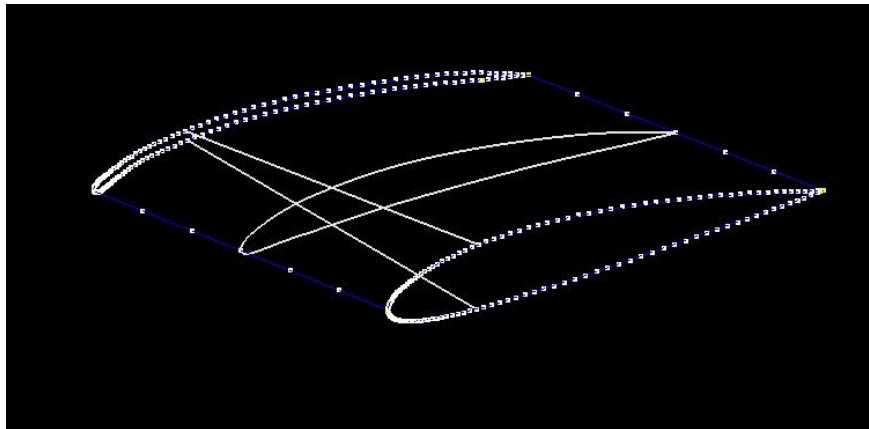


Figure 38: Interpolated grid section between NACA 2412 and Go 417a.

To accommodate the turbulence model, the y^+ values at the rotor surfaces for both grids were below 1. Figure 39 displays the y^+ on the upper surface of the standard rotor at 1000 RPM.

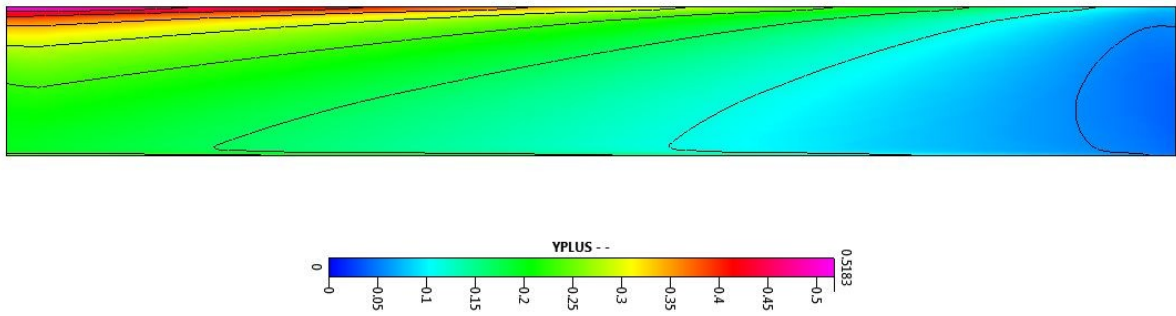


Figure 39: Y+ values on the upper surface of standard blade at 1000 RPM.

A rotating wall boundary condition was applied to the rotor walls about the hub. This allows for the effect of Ωr without the need for computationally expensive time-accurate simulations and rotating grids. To further simplify the simulations, the hub and blade tips were not discretized as the purpose of this analysis was to quantify the performance of the sectional blade geometries. Both rotors were run at 1000, 3000, and 5000 RPM to examine the effects of a large range of Reynolds numbers. Albeit high-fidelity simulations for the rotor blade surfaces, these simulations do incorporate the following assumptions:

- The rotor hub does not affect comparative results between the two blades and are not simulated for simplicity.
- Tip losses do not affect comparative results between the two blade geometries. The volume beyond the rotor tip was not discretized due to limited computational power. It is expected that any results will be an overestimate due to this.
- Wake is not considered or resolved for. This would require ultra-high fidelity grids and time accurate simulations.
- Inflow does not affect comparative results between the two blade geometries. The boundary conditions for vertical velocity were set to 0.

6.2 CFD RESULTS

Pressure contours on the upper surfaces of both geometries for all 1000, 3000, and 5000 RPM are shown in Figures 40, 41, and 42, respectively.

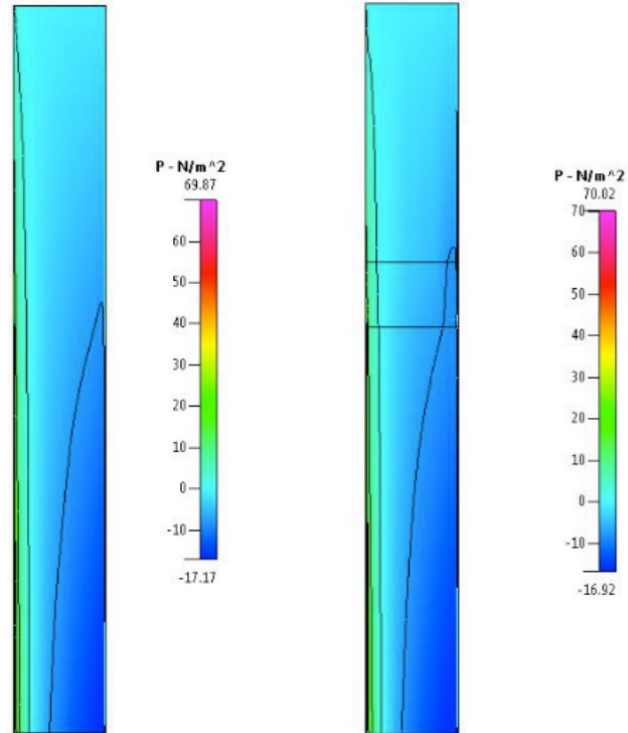


Figure 40: Pressure contours on upper surfaces of standard (left) and hybrid (right) rotors at 1000 RPM.

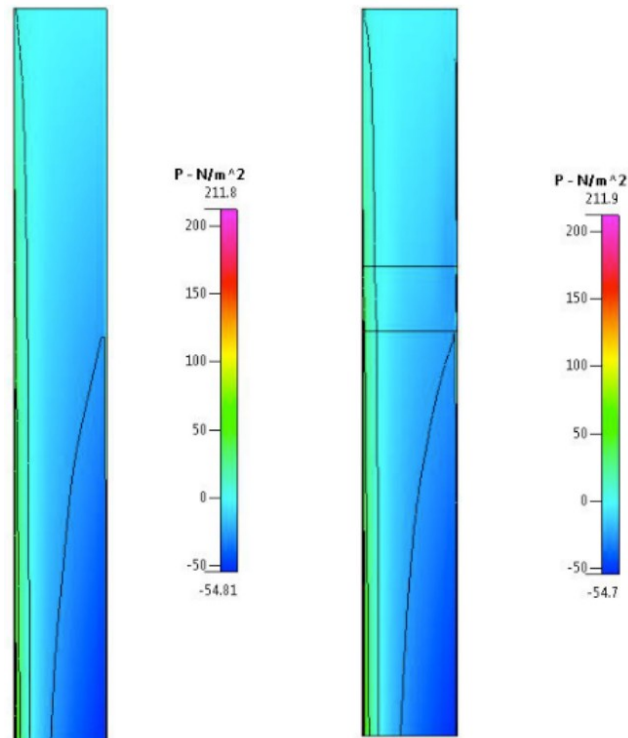


Figure 41: Pressure contours on upper surfaces of standard (left) and hybrid (right) rotors at 3000 RPM.

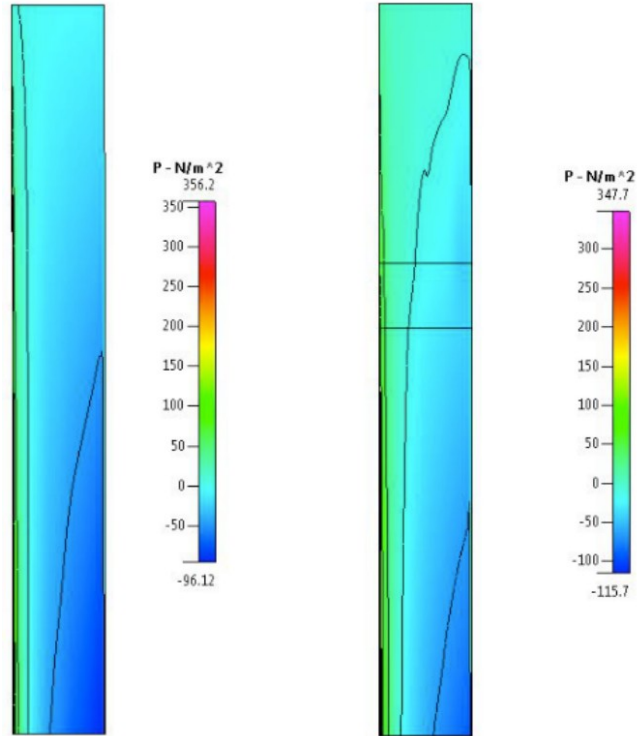


Figure 42: Pressure contours on upper surfaces of standard (left) and hybrid (right) rotors at 5000 RPM.

Velocity vectors in the field around the standard and hybrid rotors are shown in Figures 43 and 44. Note the induced inflow components around the blade caused by the rotating wall.

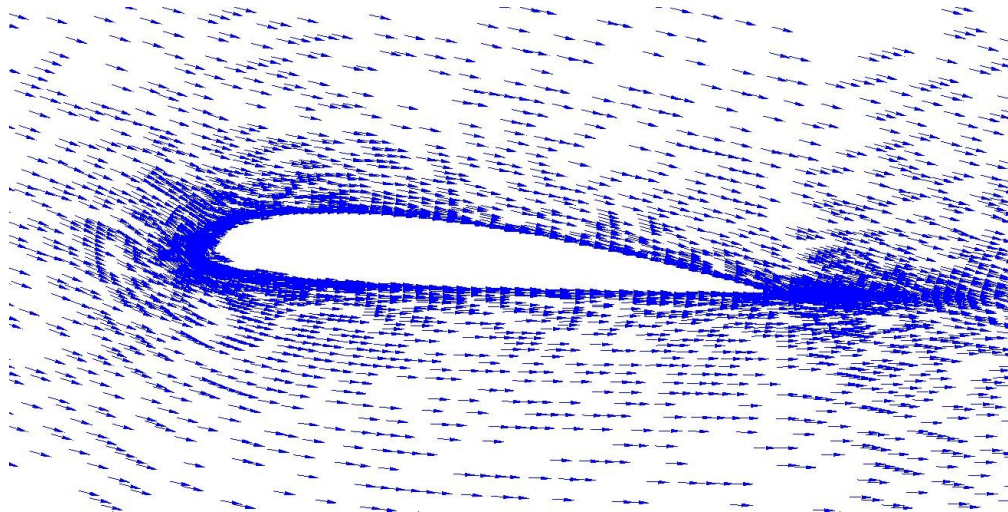


Figure 43: Velocity vectors around NACA 2412 section.

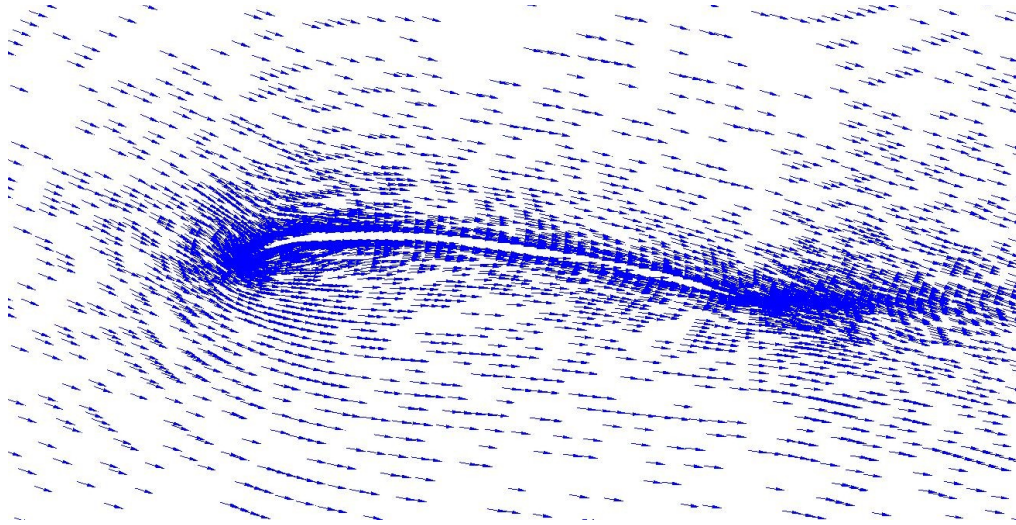


Figure 44: Velocity vectors around Goe 417a section.

For each simulation, the integrated pressure and viscous forces acting on the blade surface were combined to yield the linear vertical force and moment around the center of rotation. These two values were doubled to represent the net thrust and moment for the entire two-bladed rotor. The net moment acting against rotation was used to calculate the mechanical power required to maintain constant rotation. Equation 25 expresses mechanical power as a function of moment (τ) and rotational velocity (Ω).

$$P = \frac{\tau \times 2 \pi \times \Omega}{60} \quad (25)$$

Figure 45 shows the thrust produced by the two rotors as RPM is increases. Figure 46 expresses the thrust as a function of the mechanical power required.

Thrust vs. RPM

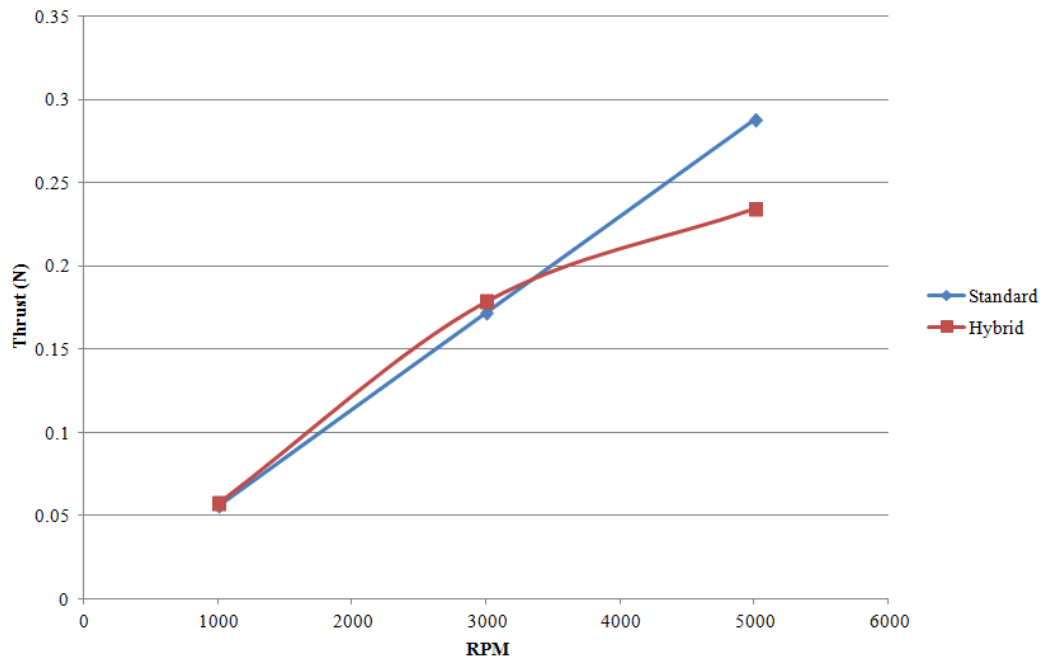


Figure 45: Thrust vs. RPM for standard and hybrid rotors.

Thrust vs. Power

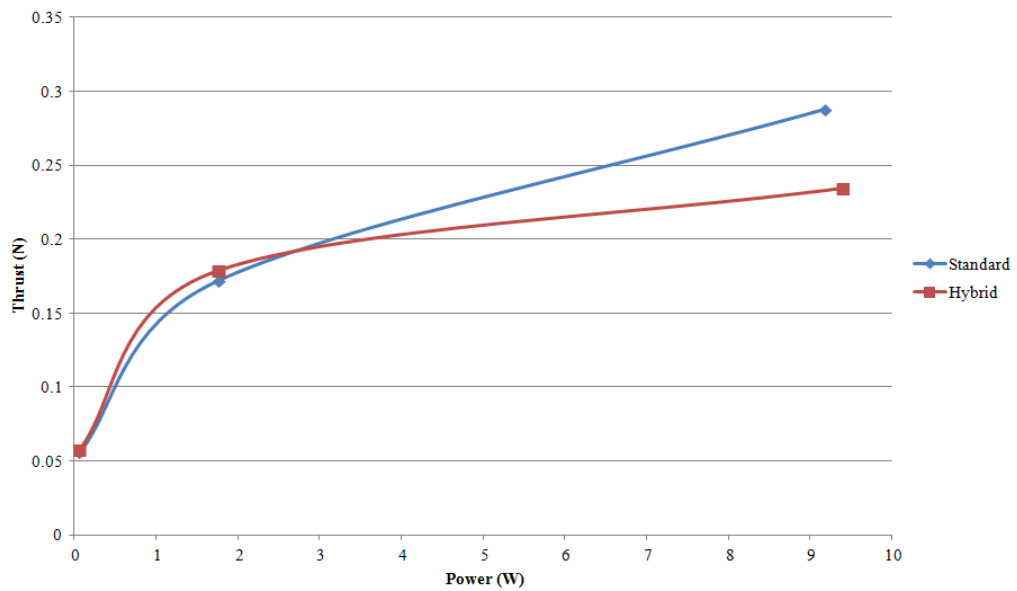


Figure 46: Predicted thrust vs. power for standard and hybrid rotors.

Although the hybrid rotor offers slightly better thrust at and below 3000 RPM the standard rotor produces noticeably greater thrust at rotational speeds above 3000 RPM. Referring to Figure 47, the hybrid rotor produces more thrust than the standard rotor for the same given

power at lower RPMs. At higher RPMs (and accordingly higher power required), the standard rotor provides superior performance. Figure 48 shows the Reynolds number the (applicable to both 1" chord standard and hybrid rotors) experienced at increasing radial stations at 3000 RPM.

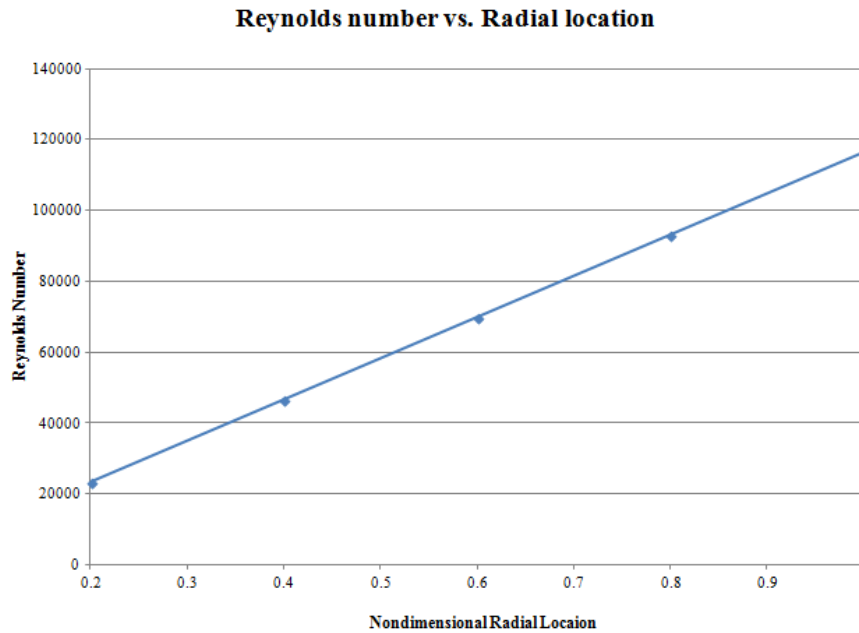


Figure 47: Reynolds number as a function of radial location for the 16.8" at 3000 RPM.

At 3000 RPM, the hybrid rotor slightly outperforms the standard rotor. Referring to Figure 48, only the outermost portion of the rotor is operating at Reynolds numbers greater than 100000. The remaining inboard portion, including the inner 40% span comprised of the Goe 417a section, is operating well below the Reynolds number limit of 100000. This data, along with the research in Section 4.4 that indicates improved aerodynamic performance of cambered-plate airfoils over traditional streamlined airfoils at Reynolds numbers below 100000, supports the resulting performance advantage the hybrid rotor offers at 3000 RPM.

7.0 EXPERIMENTAL ROTOR TESTING

Physical models of the 16.8" diameter rotors simulated in Section 6.2 were 3D printed and tested. With the exception of the rotor hub, the geometry of the standard and hybrid rotors were consistent to best experimentally validate the CFD results. A COTS 4.7° pitch rotor was additionally tested as a performance benchmark. These three rotors are described in Table 2 and shown in Image 4. A 880Kv motor as described in Section 2 was used to rotate the rotors at desired speeds. A digital scale was used to measure the torque produced by the rotor. A variable DC power supply provided the requisite voltage to the motor controller. Current to the motor controller was measured by the power supply and verified by a multimeter in series between the power supply and motor controller. The motor/rotor assembly was mounted to one end of a simple lever such that its upwards thrust is converted into a downwards force on the digital scale.

A free body diagram of this setup is illustrated in Figure 48. This actual apparatus is shown in Image 5.

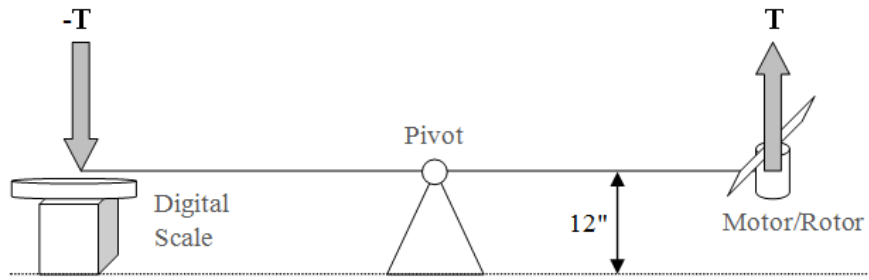


Figure 48: Free body diagram of lever apparatus to measure thrust. All rotors tested were 12" above the surface.

Table 2: Summary of rotor characteristics.

Rotor	Diameter (in)	Hub Diameter (in)	Chord (in)	Solidity	Collective (deg)
Benchmark	11	0.5	Variable	0.114	4.8°/inch twist
Standard	16.8	1	1	0.0758	4.7
Hybrid	16.8	1	1	0.0758	4.7



Image 4: Top to bottom: benchmark rotor, hybrid rotor, and standard rotor.



Image 5: Lever apparatus to measure thrust. The upwards thrust from the motor/rotor on the right side is converted into a downwards force to the digital scale on the left side.

7.1 EXPERIMENTAL RESULTS

The throttle setting on an RC transmitter was steadily increased to correspondingly increase the rotor RPM at a constant input voltage of 16.8V. The measured instantaneous current was used to obtain power consumed. A continuous loss of 0.03A due to the motor controller, receiver, and connections was factored into the calculations. Figure 49 shows the measured thrust for the three rotors as power is increases. It should be noted that value of power measured in this experiment is electrical power, not mechanical power as in the previous sections. Although the current loss of 0.03A was taken into account, the values for measured electrical power will differ from those estimated by BEM and CFD.

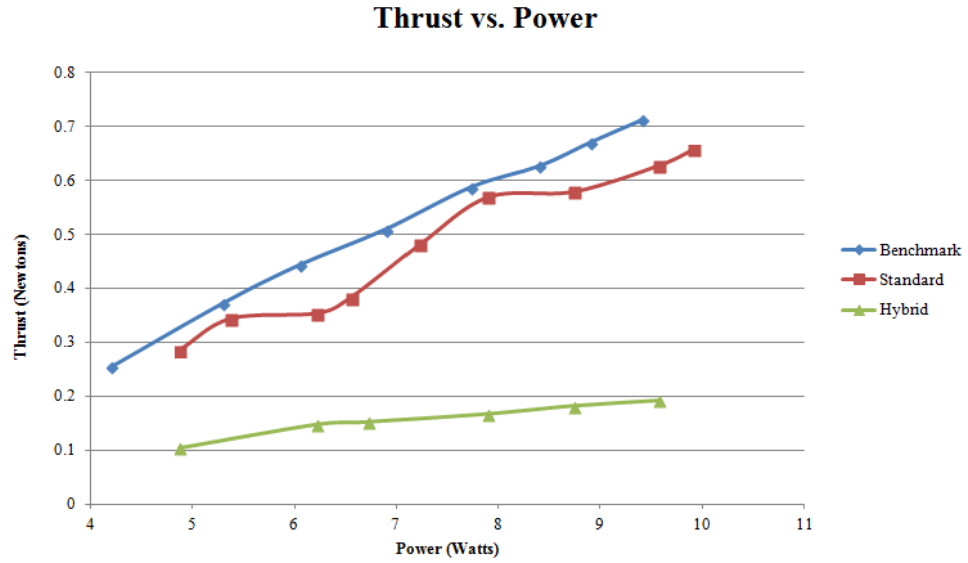


Figure 49: Measured thrust for increasing input power for the benchmark, standard, and hybrid rotors.

To account for the different diameters between the benchmark rotor and the standard and hybrid rotors, disk loading was also plotted over power and is shown in Figure 50.

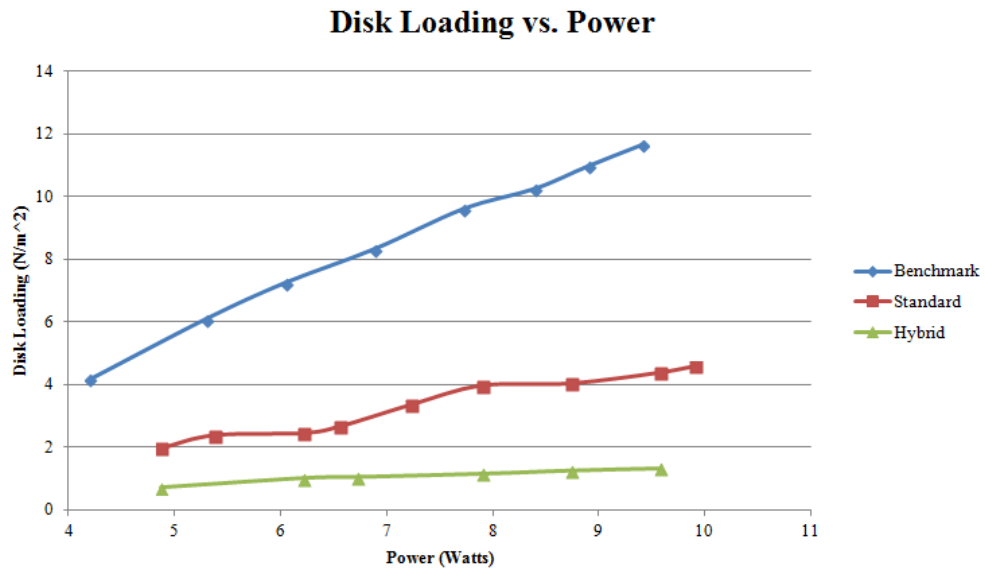


Figure 50: Disk loading on tested rotors for increasing values of electrical power.

The benchmark rotor clearly provides better overall performance than the standard and hybrid rotors. The large deficit in performance of the hybrid rotor is most likely due to the unanticipated flexing of the blade. The inner Goe 417a portions of the hybrid rotor did not provide the structural rigidity necessary to maintain a constant pitch as rotational velocity increased. A pitch-down moment from the blade's incident velocity created a near-zero angle of attack and resulted in an overall decreased thrust. This behavior was visually noted during the test of the hybrid rotor. The testing comparing these three rotors was limited to lower rotational speeds due to the structural flexibility (primarily too low torsional stiffness) of the hybrid rotor and concern over its structural robustness.

Testing comparing only the benchmark and standard rotors was continued at higher speeds to evaluate performance at higher Reynolds numbers. The results of this test are in Figure 51.

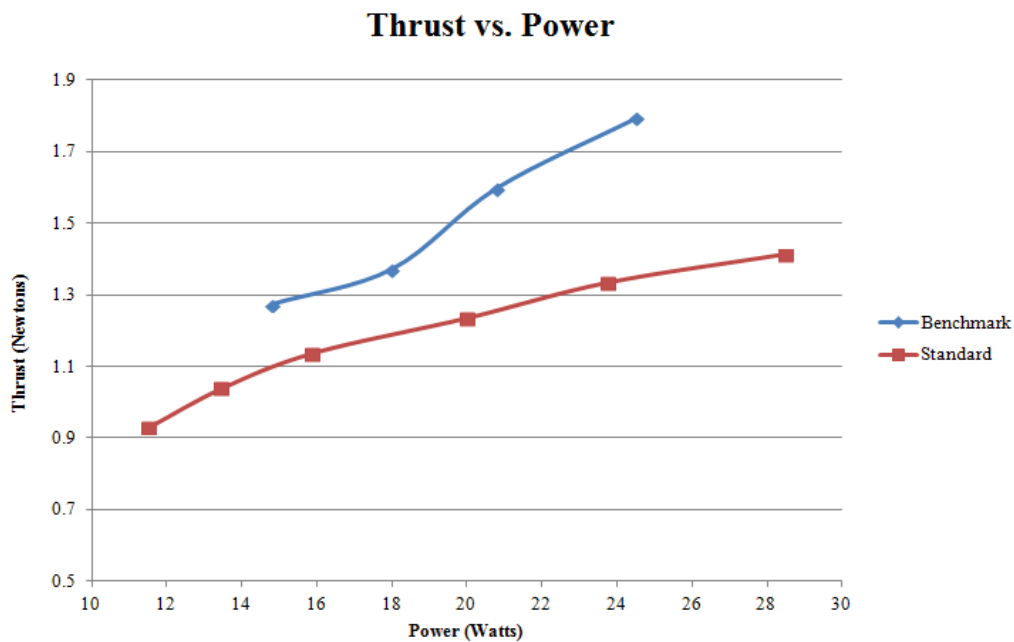


Figure 51: Performance comparison between the benchmark and standard rotors at higher rotational speeds.

To best compare the rotor performance between the predicted CFD values and the experimental measurements, both datasets are overlaid in Figure 52.

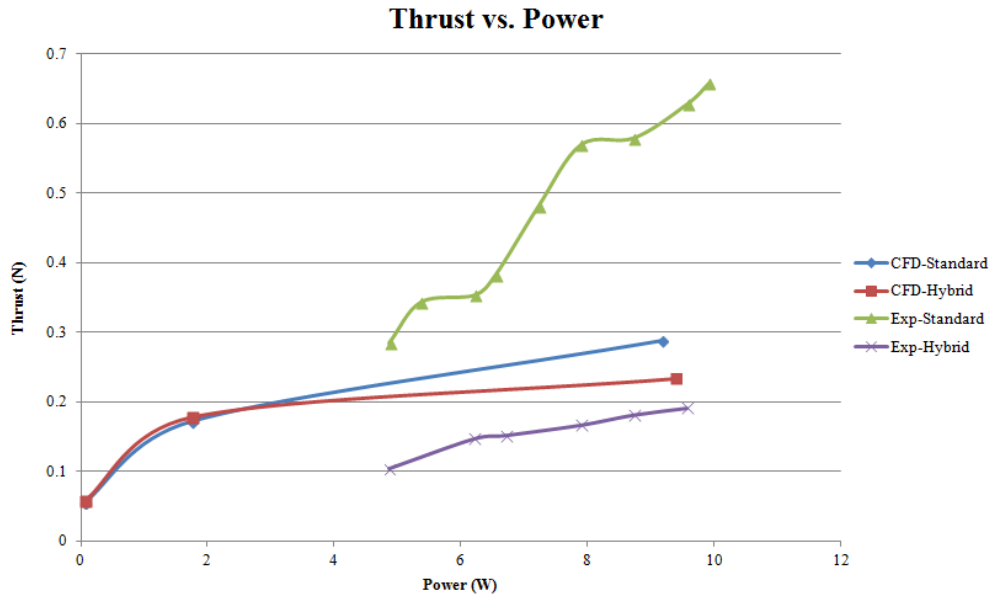


Figure 52: Thrust vs. power required plot comparing CFD and experimental results.

Referring to Figure 51, there is a consistent ~10% performance advantage of the heavier disk loaded benchmark rotor over the standard rotor. Unlike the standard rotor, the benchmark rotor incorporates factors of twist and taper in its design, furthering its potential for greater aerodynamic efficiency. The benchmark rotor's blades are also comprised entirely of cambered plate airfoils with sharp leading edges.

The experimental results for the standard rotor in Figure 52 shows an under prediction of thrust by CFD when compared to the experimental values. As noted earlier, there is an expected discrepancy between the estimated mechanical power and the measured electrical power required to maintain the rotor at a constant rotational velocity. There are several factors that possibly contribute to this discrepancy between the predicted and experimental results:

- The rotors in experimental testing may benefit from ground effect. Given that the rotors tested range from 11" to 16.8" in diameter and the motors were housed 12" above the testing surface, the impact of ground effect is entirely plausible.
- Because of the relatively large diameter, constant pitch (collective), and being constructed of a marginally rigid material, there was a small but observable coning behavior to the standard rotor as rotational velocities increased.
- A tachometer was not available to directly measure rotational velocity during the experimental testing. Thus, a precise comparison between CFD and experimental results at specified RPMs cannot be realized. Accordingly, the discrepancy in power definition and lack of measured RPM may elude to the experimental curves being "shifted" either left or right in Figure 52. The absence of rotational velocity also inhibits the calculation of Reynolds number.

- The CFD simulations were comprised of one turbulence model and one grid per geometry. Further turbulence, separation, and grid dependence studies may have produced different results.

8.0 CONCLUSIONS

This study tackled several different aspects of small rotorcraft design and development. First, a novel field telecom relay mission was outlined. Second, the preliminary design of an electric quadrotor to perform this mission was defined. Third, theoretical, numerical, and experimental investigations into the vehicle's rotor aerodynamics were performed.

The integration of more aerodynamically efficient rotors could extend hovering endurance. The experimental and computational research focused on the vehicle rotors conducted in this paper suggests a small potential performance gain when flat/cambered-plate are used for inboard blade rotor sections when operating at lower RPMs/Reynolds numbers. Implementing a transition model in the CFD simulations would have further increased physical fidelity and shown any affects of separation at the lower Reynolds portions of the blade. Because of the flexing behavior of the hybrid rotor, a true comparison between it and the standard rotor is still lacking. Both the standard and hybrid rotor were designed strictly for a performance comparison between the two and the influence of an integrated cambered plate region. Thus, these blades were not designed to maximize individual performance at their respective disk loading the comparison between them and the benchmark rotor is for qualitative value. The use of a stiffer material in the construction of the hybrid rotor may have experimentally validated its small gain. It is also worth noting that while the scope of the work in this paper focused on increasing hover endurance, there is a potential penalty for maneuverability its implications on the optimal objectives when flying rotors of low disk loading.

Further development of the proof-of-concept model was not continued due to time constraints. The hardware and framework is in hand for potential development in the future.

TO CONCLUDE

A man-portable, rapidly-deployable, and cost-effective platform to carry the TCCR or comparable communication relay will be propitious in LOS denied situations. A quadrotor is the most robust platform and will fit the required dimensional constraints of a backpack. The theoretical design and POC will utilized proven and cost-effective off-the-shelf propulsion components. The required endurance will come from the larger than average rotor diameter and custom designed blades rather than increased battery capacity. The endurance estimates in Section 2.5 neglect time to ascend to altitude which requires significant power, leaving the values an overestimate. For a set rotor geometry and propulsion, increasing battery count has diminishing returns for prolonging endurance. BEM showed a possibility for increased performance at lower RPMs using flat plate rotors near the hub. CFD simulations similarly verified that cambered plate sections near the hub provides performance benefits. Experimental

testing yielded superior performance of the off-the-shelf flat-plate rotor over the larger diameter standard and hybrid rotors. Structural limitations inhibited direct comparisons between the standard and hybrid rotors.

REFERENCES

1. Bohorquez, F., Samuel, P., Sirohi, J., Pines, D., & Rudd, L. (n.d.). *Design, analysis and performance of a rotary wing mav*. Informally published manuscript, Smart Structures Laboratory, Alfred Gessow Rotorcraft Center Department of Aerospace Engineering, University of Maryland, Johns Hopkins University/Applied Physics Laboratory.
2. Duranti, S., Conte, G., Lundstrom, D., Rudol, P., Wzorek, M., & Doherty, P. (n.d.). *Linkmav, a prototype rotary wing micro aerial vehicle*. (Master's thesis, Linköping University, SE-58183 Linköping, Sweden).
3. Mueller, T. J. (n.d.). *Aerodynamic measurements at low Reynolds numbers for fixed wing micro-air vehicles*. Informally published manuscript, Department of Aerospace and Mechanical Engineering, University of Notre Dame Notre Dame, IN 46556 USA.
4. Young, L. A., Johnson, J. L., Demblewski, R., Andrews, J., & Klem, J. (n.d.). *New concepts and perspectives on micro-robotcraft and small autonomous rotary-wing vehicles*. 20th AIAA Applied Aerodynamics Conference, St. Louis, MO, June 24-27, 2002.
5. US NAVY. (n.d.). *lieutenant michael p. murphy united states navy (seal) may 7, 1976 - june 28, 2005*. Retrieved from <http://www.navy.mil/moh/mpmurphy/bio.html>
6. Monico, G. (2012). Tactical compact communications relay (TCCR). Boeing Electronic & Mission Systems.
7. Bohorquez, F. (2007). *Rotor hover performance and system design of an efficient coaxial rotary wing micro air vehicle*. (Unpublished doctoral dissertation).

8. Sankar, Lakshmi. "Rotorcraft Aerodynamics." *Rotorcraft Aerodynamics*. N.p., n.d. Web. 08 Feb. 2013.
9. ESI CFD Inc. (2009). Cfd-Ace modules manual. Huntsville, AL:
10. Bell, S. (2008). Analysis of a rotor blade system using blade element momentum theory. In *Function to calculate the Power, Thrust and Figure of Merit of a rotor system*. [MATLAB] Retrieved from <http://www.mathworks.com/matlabcentral/fileexchange/21994-analysis-of-a-rotor-blade-system-using-blade-element-momentum-theory>
11. 3DRobotics. (2012, 11 8). *The apm 2 board*. Retrieved from <https://code.google.com/p/ardupilot-mega/wiki/APM2board>
12. Arledge, S. (Photographer). (2012, 12 4). Scan Eagle UAV [Web Photo]. Retrieved from http://commons.wikimedia.org/wiki/File:Scan_Eagle_UAV.jpg
13. Kabel, M. (Photographer). (2010, 6 12). Schiebel Camcopter S-100 [Web Photo]. Retrieved from http://commons.wikimedia.org/wiki/File:Schiebel_Camcopter_S-100_at_ILA_2010.jpg
14. Yarbrough, B. (Photographer). (2013, 3 4). :RQ20A-130304-M-DE426-001 crop [Print Photo]. Retrieved from http://commons.wikimedia.org/wiki/File:RQ20A-130304-M-DE426-001_crop.jpg
15. Hoffmann, G. (Photographer). (2007, 1 15). Schematic of reaction torques on each motor of a quadrotor aircraft, due to spinning rotors [Print Photo]. Retrieved from http://commons.wikimedia.org/wiki/File:Quadrotor_yaw_torque.png